The road to laser cooling rubidium vapor

Thomas Stark

Senior Thesis in Physics

Submitted in partial fulfillment of
the requirements for the degree of
Bachelor of Arts

Department of Physics
Middlebury College
Middlebury, Vermont

May 2011

Abstract

Laser cooling experiments developed in the last decade enable physicists to slow down and spatially confine neutral atoms of a gas, thus lowering the temperature of trapped atoms into the μK range. One of the challenges associated with laser cooling is to stabilize a laser so that its output frequency matches that of a hyperfine structure transition and has an absolute stability of several MHz. In this project, we establish the groundwork for future laser cooling experiments with ^{85}Rb by performing saturated-absorption Doppler-free spectroscopy studies. We acquire Doppler-free spectra of ^{85}Rb that resolve individual hyperfine structure transitions, including the transition that the laser must excite in laser cooling experiments. The spectra we obtained can readily be repeated and the experimental apparatus can provide the feedback for an electronic laser stabilization circuit.

Committee: _____
Anne Goodsell

_____
Jeffrey S. Dunham

_____
Roger Sandwick

Date Accepted: _____

Acknowledgments

Thank you, Bob Prigo, for getting me hooked in PHYS 0109. Thank you, Noah Graham, for thinking that every question I asked was a good one; that was very kind of you. Thank you, Steve Ratcliff, for the killer operator. Thank you, Jeff Dunham, for your seemingly infinite wisdom, red ink, and Doppler-free spectroscopy expertise. Thank you, Susan Watson, for always making me ponder subtle points and scratch my head over physical insights. Thank you, Rich Wolfson, for ensuring that I never (intentionally) equate a scalar with a vector ever again. Thank you, Lance Ritchie, for helping get the Goodsell lab up and running. Thank you, Anne Goodsell, for making this project more enjoyable and rewarding than I could have hoped. Your evident love of teaching, commitment to your students, and infectious enthusiasm will make for a long, fruitful career at Middlebury.

Thank you to my friends for the Midd Gap rides, runs, gym time, emotional support and, hence, for my mental and physical health. Thank you to my fellow physics majors for helping me survive the trials of this major. Thank you, Allie, Andrew, Sam, and Steve, for always being most-excellent. Thank you, Mom and Dad, for all of your advice and just the right amount of pressure.

Contents

List of Figures

Chapter 1

Introduction

Steven Chu,[1] Claude Cohen-Tannoudji,[2] and William Phillips,[3] jointly received the 1997 Nobel Prize in Physics for developing experiments that cool down and spatially confine the atoms of a gas. In the last decade, laser cooling has become a hot topic in experimental physics and neutral atoms have been cooled using these methods to temperatures of merely 1 μK.[1] This senior thesis work marks the beginning of a project whose goal is to laser cool 85-rubidium.

Our goals for this senior thesis project are somewhat less lofty than winning the Nobel Prize or even laser cooling ^{85}Rb within the year. The road to laser cooling is a long one and we establish crucial groundwork in the laboratory and strive to understand the theory and physical concepts underlying our experiments. The first step down the road is to understand the function of a diode laser, to which end we devote Chapter 3. Diode lasers are used in laser cooling experiments for their narrow linewidth and tunability. Using a tunable laser is a distinct advantage, as it can be tuned to match the energy of an atomic transition that is targeted in laser cooling.

While diode lasers have tunable frequency output, they can also have somewhat unstable frequency output. Hence, it is necessary to assemble an electronic feedback

[1]Stanford University, Stanford, CA. Currently U.S. Secretary of Energy.
[2]College of France, Paris, FRA
[3]National Institute for Standards and Technology, Gaithersburg, MD

circuit that stabilizes the output frequency of the laser. In this project, we obtain Doppler-free saturated-absorption spectra of the ^{85}Rb $5S_{1/2} \rightarrow 5P_{3/2}$ transition that resolve individual hyperfine transitions and will be used as the feedback for laser stabilization in the future. Chapter 4 outlines the theory behind the experimental techniques used, and Chapter 5 describes our experimental setup and results.

In Chapter 2, we explore some results regarding the interaction of light and matter that will be useful in later chapters. Chapter 6 describes the theory behind laser cooling. This chapter may be of use to future thesis students as a means of understanding the ultimate goals of the project. The reader may also want to read this chapter first, as motivation for the measures taken throughout this project.

Chapter 2

Light and Matter

2.1 The Electric and Magnetic Wave Equations

In 1861, James Clerk Maxwell published *On Physical Lines of Force*, a paper that featured a set of equations to describe electromagnetic phenomena. Although Maxwell drew from the work of Michael Faraday, André-Marie Ampère, and Carl Gauss, the equations are now unified under the name "Maxwell's equations" to credit Maxwell's astute realization of the need to augment Ampère's Law. Maxwell also postulated the existence of electromagnetic waves in *A Dynamical Theory of the Electromagnetic Field* in 1864. In this view, light could now be seen as an electromagnetic phenomenon.

In laser cooling experiments, we are particularly concerned with the ways in which electromagnetic radiation interacts with matter. In particular, we must be familiar with light propagating through dielectric media, such as a dielectric solid or a gas of neutral atoms, such as rubidium vapor. In a dielectric medium, Maxwell's equations become [2]

$$\vec{\nabla} \cdot \vec{D} = 0 \tag{2.1}$$

$$\vec{\nabla} \cdot \vec{B} = 0 \tag{2.2}$$

$$\vec{\nabla} \times \vec{E} = -\frac{\partial \vec{B}}{\partial t} \tag{2.3}$$

$$\vec{\nabla} \times \vec{H} = \frac{\partial \vec{D}}{\partial t}. \tag{2.4}$$

We will be concerned with nonmagnetic media, in which $\vec{H} = \frac{1}{\mu_0}\vec{B}$. The electric displacement $\vec{D}$ is proportional to the electric field $\vec{E}$ and the medium's electric polarization $\vec{P}$: [1]

$$\vec{D} = \epsilon_0 \vec{E} + \vec{P}. \tag{2.5}$$

It will be useful in later discussions (Chapter 4) to express the wave equation for electromagnetic radiation in dielectric media. To do so, we first take the curl of both sides of Faraday's Law (Eq. 2.3)

$$\vec{\nabla} \times \left(\vec{\nabla} \times \vec{E}\right) = -\vec{\nabla} \times \frac{\partial \vec{B}}{\partial t}.$$

The triple product on the left hand side can be rewritten and Ampère's Law (Eq. 2.4) can be used to express the right hand side in terms of the electric displacement:

$$\vec{\nabla}\left(\vec{\nabla} \cdot \vec{E}\right) - \nabla^2 \vec{E} = -\mu_0 \frac{\partial^2 \vec{D}}{\partial t^2}.$$

Substituting for the electric displacement, using Eq. 2.5, and rearranging terms, we find that

$$\nabla^2 \vec{E} - \vec{\nabla}\left(\vec{\nabla} \cdot \vec{E}\right) - \frac{1}{c^2}\frac{\partial^2 \vec{E}}{\partial t^2} = \frac{1}{\epsilon_0 c^2}\frac{\partial^2 \vec{P}}{\partial t^2}.$$

[1] I refer to $\vec{P}$, the electric dipole per unit volume of the medium, as the "medium's polarization" in order to differentiate it from the polarization of an electromagnetic wave.

Here, we have invoked the relationship $\frac{1}{\mu_0 \epsilon_0} = c^2$ in order to introduce the speed of light in vacuum c and massage this expression to take on the recognizable form of the wave equation. If we consider only transverse fields, then $\vec{\nabla} \cdot \vec{E} = 0$ and the electric wave equation is

$$\nabla^2 \vec{E} - \frac{1}{c^2} \frac{\partial^2 \vec{E}}{\partial t^2} = \frac{1}{\epsilon_0 c^2} \frac{\partial^2 \vec{P}}{\partial t^2}. \tag{2.6}$$

By a similar derivation, we can express the wave equation for the magnetic field

$$\nabla^2 \vec{B} - \frac{1}{c^2} \frac{\partial^2 \vec{B}}{\partial t^2} = \frac{-1}{\epsilon_0 c^2} \frac{\partial}{\partial t} \left(\vec{\nabla} \times \vec{P} \right). \tag{2.7}$$

Maxwell's equations have yielded a powerful result. Equations 2.6 and 2.7 reveal that electric and magnetic fields propagate through dielectric media as a wave.

This formulation of the wave equation relates information about how electric and magnetic fields propagate through a dielectric to material properties of the dielectric. The polarization $\vec{P}$ in Eq. 2.6 is the dipole moment per unit volume of matter. In the presence of an electric field, the electron cloud and the nucleus of an atom will experience oppositely directed forces in accordance with the Lorentz force law, causing the atom to separate spatially into a region of positive charge and a region of negative charge: an electric dipole. The electric dipole moment $\vec{p}$ of an atom is proportional to the electric field that the atom experiences: $\vec{p} = \alpha \vec{E}$. The proportionality constant α is called the atomic polarizability and it is an atomic property that can be predicted from the quantum mechanics of the atom. In order to fully understand the relationship given by the wave equation, we will commit Chapter 4 to studying these material properties. In examining a semiclassical model of the atom called the Lorentz model, we will find that α is actually dependent upon the frequency of the incident electric field. This will be an important consideration when we are performing spectroscopic studies of rubidium.

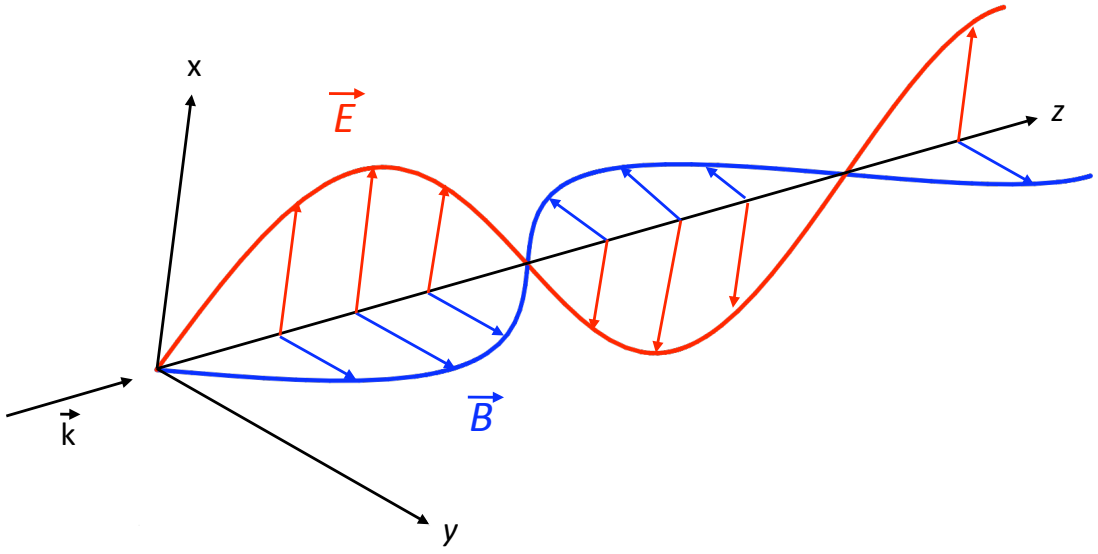

Figure 2.1: Diagram of a monochromatic plane wave polarized in the $\hat{x}$ direction and propagating in the $\hat{z}$ direction.[3]

2.2 Polarization of Light

The polarization of a wave is the direction of the wave's displacement from equilibrium. For a wave on a piece of rope, for example, the polarization is the direction that a fixed point on the rope moves over time. By convention, the polarization of an electromagnetic wave is taken to be the direction of the electric field. For example, Fig. 2.1 shows light polarized in the $\hat{x}$ direction, traveling with wave vector $\vec{k} = k\hat{z}$.[2] Vertical polarization is a term often used to indicate polarization in the direction perpendicular to the surface of an optics table. Likewise, horizontal polarization indicates polarization in the direction parallel to the table surface.

In general, the complex exponential form for the electric field of an electromagnetic

[2]For consistency throughout this document, we will refer to an electromagnetic wave propagating in the $\hat{z}$-direction, as shown in Fig. 2.1.

wave propagating in the $\hat{z}$ direction is written

$$\vec{\tilde{E}}(z,t) = E_{0x}e^{i(kz-\omega t)}\hat{x} + E_{0y}e^{i(kz-\omega t+\delta)}\hat{y}. \tag{2.8}$$

In this expression, δ is the *relative* phase between the two waves and it suffices to include this information in the y-component of the complex electric field. Equivalently, we can rewrite this expression using Euler's formula.[3] The real part of this complex expression is the physical electric field:

$$\vec{E}(z,t) = E_{0x}\cos(kz-\omega t)\hat{x} + E_{0y}\cos(kz-\omega t+\delta)\hat{y}. \tag{2.9}$$

This is a general form for the equation of a linearly polarized electromagnetic wave. For linear polarization, the direction of the electric field vector does not change with time; it always points in the same direction in the x-y plane. If $E_{0x} = 0$, for example, the wave is polarized in the $\hat{y}$ direction. If $E_{0x} = E_{0y}$, then the wave is polarized at a 45° angle to the x-axis.

The polarization of a wave can be changed by causing one of the electric field components to become out of phase with the other. Let us consider several phase shifts to the y-component of Eq. 2.8. First, consider shifting the phase of the y-component π radians behind the x-component. Equation 2.8 becomes

$$\begin{aligned} \vec{\tilde{E}}(z,t) &= \tilde{E}_{0x}e^{i(kz-\omega t)}\hat{x} + \tilde{E}_{0y}e^{i(kz-\omega t+\pi)}\hat{y} && (2.10)\\ &= \tilde{E}_{0x}e^{i(kz-\omega t)}\hat{x} - \tilde{E}_{0y}e^{i(kz-\omega t)}\hat{y}. && (2.11) \end{aligned}$$

Here, I've used the fact that adding a phase shift of π radians is mathematically equivalent to multiplying by -1. Once again using Euler's formula and taking only

[3] $e^{i\beta} = \cos(\beta) + i\sin(\beta)$

the real part to be the electric field, we find that

$$\vec{E}(z,t) = E_{0x}\cos(kz-\omega t)\hat{x} - E_{0y}\cos(kz-\omega t)\hat{y}. \tag{2.12}$$

If the x and y components of the electric field become π radians, or 180°, out of phase with one another, the resultant polarization is still linear, but flipped about the x-axis. Therefore, for radiation polarized at an angle θ to the x-axis, a phase shift of π radians rotates the polarization by an angle of 2θ.[4] By this same logic, you could convince yourself that introducing a phase shift of $-\pi$ radians to the wave represented by Eq. 2.12 would recover the original polarization angle.

Now, let us consider introducing a phase shift of $\frac{\pi}{2}$ radians to the y-component of Eq. 2.9. In this case, Eq. 2.9 becomes

$$\begin{aligned} \tilde{\vec{E}}(z,t) &= \tilde{E}_{0x}e^{i(kz-\omega t)}\hat{x} + \tilde{E}_{0y}e^{i(kz-\omega t+\frac{\pi}{2})}\hat{y} && (2.13)\\ &= \tilde{E}_{0x}e^{i(kz-\omega t)}\hat{x} + i\tilde{E}_{0y}e^{i(kz-\omega t)}\hat{y}, && (2.14)\end{aligned}$$

where I've used the fact that $e^{i\frac{\pi}{2}} = i$. Repeating the steps of using Euler's formula and taking the real part, we find that

$$\vec{E}(z,t) = E_{0x}\cos(kz-\omega t)\hat{x} - E_{0y}\sin(kz-\omega t)\hat{y}. \tag{2.15}$$

Letting $z = 0$, it is clear that the polarization vector traces, in time, an ellipse in the x-y plane with axes of length $2E_{0x}$ and $2E_{0y}$. We are more interested in the special case in which $E_{0x} = E_{0y}$ and can see that the polarization vector traces out a circle in time in the x-y plane. If, when viewing the x-y plane from the positive z-axis, the polarization vector traces out a circle in the clockwise direction, the radiation is said to be right circularly polarized, as shown in Fig. 2.2a. Conversely, if the polarization

[4] $\theta \equiv cos^{-1}(E_{0y}/E_{0x})$

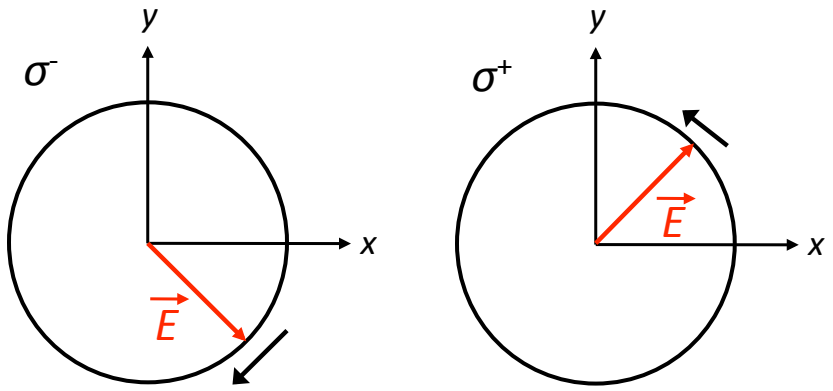

(a) Right circularly polarized light. (b) Left circularly polarized light.

Figure 2.2: Circularly polarized light.[4]

vector traces out a counterclockwise circle in the x-y plane, the radiation is left circularly polarized, as shown in Fig. 2.2b.[4][5] For $E_{0x} = E_{0y}$, Eq. 2.15 represents right circularly polarized radiation. By convention, right circularly polarized radiation is denoted σ^-, while left circularly polarized radiation is denoted σ^+.

Let us now consider the possibility of shifting the y-component of the circularly polarized wave (Eq. 2.15) by π radians behind the x-component. Mathematically, this means that

$$\vec{E}(z,t) = E_{0x}\cos(kz-\omega t)\hat{x} - E_{0y}\sin(kz-\omega t+\pi)\hat{y} \quad (2.16)$$

$$= E_{0x}\cos(kz-\omega t)\hat{x} + E_{0y}\sin(kz-\omega t)\hat{y}. \quad (2.17)$$

In this case, the polarization vector would trace out an circle in the x-y plane, but in the opposite direction as that in Eq. 2.15. Thus, a phase shift of π radians can change the direction of circular polarization.

Since electromagnetic radiation carries momentum in its fields, it should be no surprise that circularly polarized radiation carries both angular momentum and linear momentum.[3] The atom traps used in laser cooling experiments exploit this property in order to create a spatially-dependent restoring force on the atoms. Thus, the ability

to control the polarization of light is crucial to laser cooling experiments, as we will discuss in Chapter 6.

2.3 Wave Plates

When conducting experiments involving optics equipment and lasers, it is often convenient or necessary to change the polarization of radiation. For example, it may be necessary to simply rotate a linearly polarized beam, rotate vertical polarization to horizontal, circularly polarize a linearly polarized beam, or change between right and left circularly polarized radiation. We saw how this is explained mathematically in section 2.2. Now, we describe the physical devices that make such changes in polarization possible: waveplates.

Consider laser radiation of angular frequency ω_L incident upon an atom. The electric field component of the laser radiation exerts a force on the electrons in an atom. An electron in an atom can be viewed as a charged mass m_e on a spring of spring constant k_s.[5] The electron of mass m_e will then oscillate at its natural frequency:

$$\omega_0 = \sqrt{\frac{k_s}{m_e}}. \tag{2.18}$$

The oscillating electron reradiates and the incident and reradiated waves recombine in the medium. The resultant wave may be out of phase with the incident wave. We know this from intuition; the speed of light in matter is less than c because the index of refraction is greater than one. The higher the index of refraction, the more the wave slows down and the greater the phase difference.

Crystaline solids have a particular direction, determined by the crystal structure, that is called the optic axis. Some crystals are classified as optically anisotropic, meaning that their optical properties are different in directions perpendicular and

[5]We will revisit this view in section 4.2. Although the model studied there applies to dilute dielectric gases, it can be extended to dielectric solids by using the Clausius-Mossotti equation.[3]

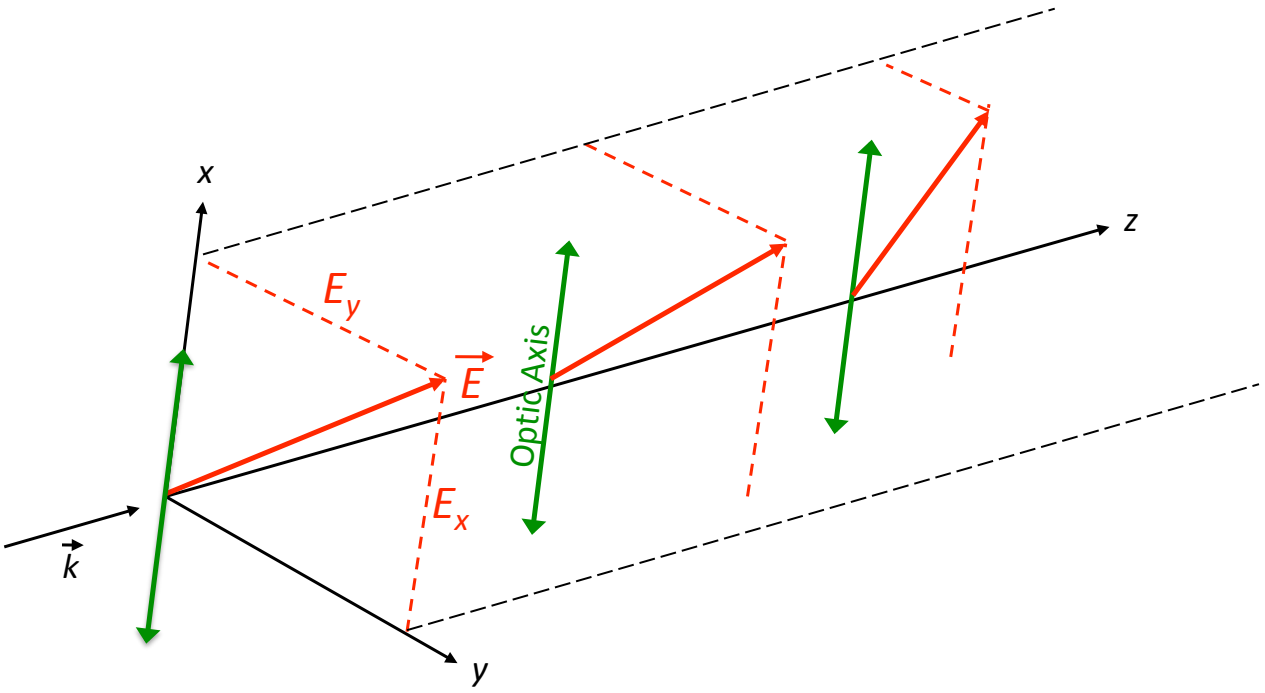

Figure 2.3: An electromagnetic wave of wavevector $\vec{k} = k\hat{z}$ and electric field polarization vector $E_x\hat{x} + E_y\hat{y}$ (red) propagating through an anisotropic medium. The crystal optic axis (green arrows) is in the $\hat{x}$-direction.

parallel to the optic axis.[6] For light traveling through an anisotropic crystal, the component of the the wave polarized parallel to the optic axis experiences a small index of refraction and is weakly absorbed by the medium. Conversely, the component of the wave polarized perpendicular to the optic axis is strongly absorbed.[7] [6]

Consider the case of an electromagnetic wave propagating through an anisotropic solid, as shown in Fig. 2.3. The wave has wavevector $\vec{k} = k\hat{z}$ and polarization in an arbitrary direction parallel to the x-y plane. If the crystal's optic axis is in the $\hat{x}$-direction, then the component of the wave polarized in the $\hat{x}$-direction will experience an index of refraction n_x that is less than n_y, the index of refraction encountered by the component of the wave polarized perpendicular to the optic axis. When the light

[6]The anisotropy of optical properties results from anisotropy of binding strengths in the crystal. Equation 2.18 provides some intuition for this; a stronger binding force can be viewed as a stiffer spring that would result in a higher natural frequency of oscillation. Again, I will refer the reader to Chapter 4 for more information on optical properties such as refractive index.

[7]It is important to note that the optic axis is a *direction* in the crystal and not a single *line*.

travels a distance z through an anisotropic crystal, the $\hat{x}$ and $\hat{y}$ components of the wave are shifted out of phase from one another by [2] [6]

$$\delta = \frac{\omega_L z}{c} \left(n_y - n_x \right). \tag{2.19}$$

We have already seen in section 2.2 how a phase difference between these two components can change the polarization. Waveplates are constructed by choosing an anisotropic solid with the desired indices of refraction n_x, n_y and making it the appropriate thickness to cause the desired phase shift. Since the phase difference also depends upon ω_L, manufacturers typically specify a range of frequencies over which the waveplate is operable. For many optics experiments, including laser cooling (Chapter 6), having control over the polarization of light is crucial.

Chapter 3

Diode Laser

3.1 Semiconductor Materials and Junctions

Crystalline solid semiconductors have electrical conductivity between that of a metal and an insulator. Their most notable electrical property is the existence of a region of energies forbidden to electrons, known as the band-gap. By altering the conductivity and layering semiconductors, a class of devices known as semiconductor junction devices can be fabricated. Semiconductors enable the creation of light emitting diodes, transistors, photovoltaic cells, and laser diodes. This section discusses the physical properties of semiconductors that enable the creation of such devices, particularly laser diodes.

The energy and linear momentum ($p = \hbar k$) of a free electron, or one in the absence of an external electrical potential, are related by

$$E(k) = \frac{\hbar^2 k^2}{2m_e}, \tag{3.1}$$

where m_e is the mass of the electron and k is the electron wave-vector. [7] [8] In a semiconductor, electrons are not free particles, nor are they bound to specific atoms or molecules within the solid. They travel through the solid and are perturbed by the

periodic potential energy produced by the crystal lattice $U(\vec{r})$.[1] The time-independent Schrödinger equation for an electron in a semiconductor is

$$\frac{-\hbar^2}{2m_e}(\frac{\partial^2}{\partial x^2}+\frac{\partial^2}{\partial y^2}+\frac{\partial^2}{\partial z^2})+U(\vec{r})\psi(\vec{r})=E\psi(\vec{r}). \tag{3.2}$$

Bloch's Theorem states that the solution to Eq. 3.2 is of the form

$$\psi(\vec{r})=U(\vec{r})e^{i\vec{k}\cdot\vec{r}}. \tag{3.3}$$

Treating the electron as a quantum mechanical particle in a cube of side length L, we impose periodic boundary conditions for the wave-vector in three dimensions

$$k_x x+k_y y+k_z z=k_x(x+L)+k_y(y+L)+k_z(z+L). \tag{3.4}$$

This requires that

$$k_x=0,\pm\frac{2\pi}{L},\pm\frac{4\pi}{L}\ldots, \tag{3.5}$$

with the same values for k_y and k_z.[8]

The band-gap arises from the fact that, at the Brillouin zone boundaries, the electron wave functions are standing waves. Consequently, $k=\frac{n\pi}{a}$, where n is an integer and a is the lattice constant of the crystal lattice. Here, k satisfies the Bragg diffraction condition, resulting in one wave traveling to the right and one traveling to the left. This results in two standing wave solutions to the time-independent Schrödinger equation, each of which concentrates electrons at different regions in space, so that each wave has a different expectation value for potential energy. The difference between these two energies is the band-gap. [8] There are no allowed energy levels for electrons within the band-gap. Above and below the band-gap, electrons occupy closely-spaced energy levels so that each band can be viewed as a single

[1] For this reason, electrons in a semiconductor are often described as "nearly free."

continuous band of energies.

Electrons with energies above that of the band-gap occupy the conduction-band, while those with energies below the band-gap occupy the valence-band. Near the bottom of the conduction-band, for $|k| < \frac{\pi}{a}$, the energy of an electron can be approximated as parabolic

$$E(k) \approx E_C + \frac{\hbar^2 k^2}{2m_e^*}, \tag{3.6}$$

where E_C is the energy of the conduction-band. Unlike a free electron, an electron in a semiconductor behaves as though it has effective mass m_e^* in the presence of the periodic potential of the crystal lattice. We can similarly describe the absence of an electron, called a hole, in the valence-band with the same quantum number k and a similar energy-momentum relation

$$E(k) \approx E_V - \frac{\hbar^2 k^2}{2m_h^*}, \tag{3.7}$$

where E_V is the valence-band energy and m_h^* is the effective mass of a hole. This shows that the band edges in a typical semiconductor can be approximated as parabolic well within the first Brillouin zone,[2] as shown in Fig. 3.1. Figure 3.1 also shows how an electron-hole pair is created when an incident photon excites an electron from the valence-band to the conduction-band. Note that the reverse process also occurs; when an electron-hole pair recombines, a photon is released. [7] This process is the basis of a laser diode, as we will discuss in the next section.

In semiconductor physics, it is useful to define a quantity called the Fermi level, E_F which is the highest energy occupied by an electron. The Fermi-Dirac distribution

$$f(E) = \frac{1}{1 + e^{\frac{E - E_F}{k_B T}}}, \tag{3.8}$$

[2]This approximation holds for $k < \frac{\pi}{a}$, or near the bottom of the conduction-band and top of the valence-band.

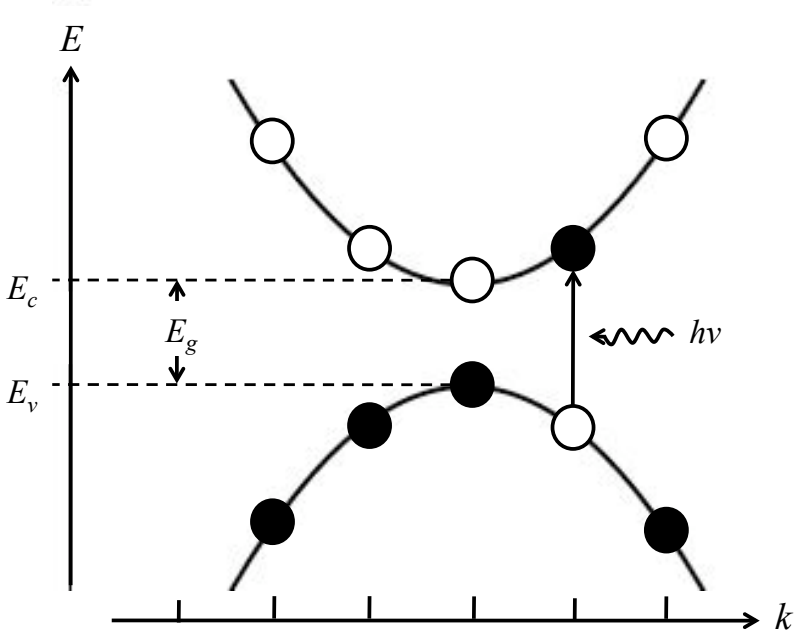

Figure 3.1: Parabolic energy bands in a semiconductor as a function of wave-vector k, away from the first Brillouin zone boundary. Dark circles represent electrons and light circles represent holes. [9]

where k_B is Boltzmann's constant, gives the probability that, at temperature T, an energy state of energy E is occupied by an electron. The probability of an electron having an energy $E > E_F$ decreases with increasing E.

According to Eq. 3.5, a single state occupies a volume of $(\frac{2\pi}{L})^3$ in k space. In k-space, an electron occupying the Fermi energy level has wave-vector k_F. We can then count the number of electron quantum states N contained in a sphere of radius k_F

$$N = 2\frac{4/3\pi k_F^3}{(2\pi/L)^3}, \tag{3.9}$$

the factor of two accounting for the two spins of the electron. Solving for k_F and plugging into Eq. 3.6, we find that

$$E_F = \frac{\hbar^2}{2m_e^*}\left(3\pi^2\frac{N}{V}\right)^{2/3} + E_C \tag{3.10}$$

where $V \equiv L^3$ is the volume of the "box" containing the electron. This says that the

Fermi level of electrons in the conduction-band depends solely on electron concentration. Thus, by changing the electron concentration in a semiconductor, we have the ability to control the Fermi level. In a laser diode, this is achieved by sending a current through the semiconductor material, as we will see in section 3.2.2. The temperature dependence of Eq. 3.10 is contained in the electron carrier concentration $\frac{N}{V} = n$ (Eq. A.4).

3.1.1 Intrinsic Semiconductors and Doping

In Appendix A,[3] we derive an expression for the intrinsic carrier concentration in a semiconductor at thermal equilibrium, for which the Fermi level lies well within the band-gap, $k_B T \ll |E - E_F|$. [9] [8] We find that the intrinsic carrier concentration can be expressed

$$n_i = 2\left(\frac{k_B T}{\hbar^2}\right)^{3/2} (m_e^* m_h^*)^{3/4} \exp\left[\frac{E_V - E_C}{2k_B T}\right]. \tag{3.11}$$

This shows that the intrinsic carrier concentration in a semiconductor does not depend upon the Fermi level. We will soon see that adding carriers to the semiconductor changes the Fermi level.

Intrinsic semiconductors, or those with no impurities, have electron and hole concentrations given by the intrinsic carrier concentration. We can change the carrier concentrations by adding electrons or holes, the process of which is called doping. Semiconductors can be p-doped by adding holes and causing the material to become an acceptor of electrons. This is achieved by introducing an impurity atom of similar lattice constant. This impurity atom has fewer valence electrons than the pure semiconductor atoms, resulting in a deficiency of electrons when chemical bonds form. For example, if boron (valence three) is added to pure silicon (valence four), then a

[3] Although similar derivations can be found in refs. [9] or [8] and may be addressed in a course such as PHYS 340 or 350, a concise derivation is provided here.

hole is left over after boron forms tetrahedral bonds with the nearest-neighbor silicon atoms. This semiconductor now has a mobile positive charge and will readily accept an electron. This has a profound impact on the electrical conductivity of the material; silicon with boron added in just 1 part in 10^5 has a conductivity 1,000 times that of intrinsic silicon at room temperature [8].

Similarly, an n-doped semiconductor is made by adding electrons and causing the semiconductor to become an electron donor. Adding an electrically neutral impurity atom with a greater number of valence electrons to the intrinsic semiconductor crystal lattice results in extra free electrons within the lattice. For example, the group IV element silicon has the same crystal structure as diamond, forming a tetrahedral bonds with its nearest neighbors. Introduction of phosphorus, valence five, results in one extra electron after the four bonds with nearest neighbor silicon atoms have been formed. Thus, these doped atoms can readily give up an electron and are said to be electron donors.

When semiconductors are moderately doped, the concentration of dopant electrons approximately equals the intrinsic electron concentration. Knowing the electron concentration, the law of mass action (Eq. A.9) can be used to find the conduction electron concentration in terms of the dopant concentration. The calculation is similar for dopant holes and the resultant valence-band hole concentrations. For moderate doping, the Fermi level is unchanged. When a semiconductor is heavily doped, however, the Fermi level can be raised into the conduction-band for n-doping or lowered in energy to the valence-band for p-doping. In this case, the Fermi level is no longer in the band-gap and the thermal equilibrium approximation (Eqs. A.3 and A.5) fails.

The condition of heavy doping creates electron-hole pairs. Electrons-hole pairs can annihilate through radiative or nonradiative recombination. Radiative recombination occurs in direct band-gap semiconductors, in which the minimum of the conduction-band and the maximum of the valence-band occur at the same value of k. In radiative

recombination, the energy released is in the form of radiation with $h\nu = E_G$, as shown in Fig. 3.1. Nonradiative recombination occurs in indirect band-gap semiconductors and is undesirable in semiconductor applications such as diode lasers. Here, energy is released in the form of a phonon, which dissipates as vibration and heat in the solid. In a heavily doped semiconductor, electrons and holes recombine at a rate far slower than the time it takes for thermal equilibrium to be reached within each band. Thus, the holes in the valence-band are at thermal equilibrium, as are the electrons in the conduction-band, yet the electrons and holes are not in thermal equilibrium with each other. The semiconductor is said to be in a state of quasi-equilibrium. At quasi-equilibrium, we refer to the semiconductor as having two separate Fermi levels for the conduction-band electrons E_{F_e} and for the valence-band holes E_{F_h}. We are particularly interested in the role of radiative recombination in the function of a laser diode and will revisit this topic in section 3.2.

3.1.2 Semiconductor Junctions

A homojunction is a semiconductor device that is formed when regions of the same semiconductor with different levels of doping are brought into contact. Many interesting applications arise from a configuration in which a region of n-doped semiconductor interfaces with a region of p-doped semiconductor, known as a p-n junction. At a p-n junction, carriers diffuse from regions of high concentration to low concentration in the form of a diffusion current. Electrons in the conduction-band recombine with holes in the valence-band, leaving behind positively charged, immobile ions. Similarly, holes in the valence-band recombine with electrons in the conduction-band, leaving behind negatively charged, immobile ions. This leaves a narrow region on either side of the junction that is depleted of mobile charge carriers. This region, known as the depletion layer, has a thickness that is inversely proportional to the dopant concentration.[7]

Now, the junction has a region of immobile positive charge on the n side and a region of negative charge on the p side. This results in an electric field pointing from the n-region to the p-region, preventing further diffusion of mobile charge carriers. Once equilibrium has been achieved, the n side is at a higher electrostatic potential than the p side, resulting in a lower potential energy for electrons in the n-region. This band bending occurs until the solid is in thermal and electrical equilibrium and has a single Fermi level. [7]

The p-n junction can be forward biased by applying a positive voltage to the p-region and grounding the n-region. This produces an electric field from the p-region to the n-region, opposite in direction to that created by the semiconductor at equilibrium. Electrons flow from the n-region to the p-region, while holes flow from the p-region to the n-region. Forward biasing disrupts equilibrium and the electrons and holes have two separate Fermi levels, $E_{F_e} > E_{F_h}$. The semiconductor is now in a state of quasi-equilibrium. [7]

3.2 The Laser Diode

The properties of semiconductors that have been described thus far lend themselves to applications in which electrical energy is transformed into radiation or radiation energy is turned into an electrical signal. Laser diodes and LED's are an example of the former, while the photodetector is an example of the latter. This section discusses how the properties of semiconductors lend themselves to the creation of a laser, which is an acronym for light amplification by stimulated emission of radiation.

3.2.1 Population Inversion, Stimulated Emission, and Gain

In stimulated emission, a photon incident upon an electron that has been excited to the conduction-band causes the electron to recombine radiatively with a hole. The

photon released is of identical wave-vector $\vec{k}$, frequency, polarization, and phase.[9] In a semiconductor at thermal equilibrium, this process would necessitate sending in an incident photon to create an electron-hole pair, then subsequently sending in a photon to cause emission. In this photon-for-photon trade, there would be no net increase of photons in the semiconductor material.

Increasing the number of emission events in the semiconductor first requires the creation of many electron-hole pairs. This means raising the quasi Fermi level for electrons into the conduction-band, lowering the Fermi level for holes into the valence-band, or both, and can be accomplished by forward biasing the junction. We will soon see that this sufficient forward biasing enables stimulated emission.

When photons interact with electron-hole pairs in a semiconductor, energy and momentum must be conserved. Energy conservation dictates that the energy of an absorbed or emitted photon must equal the separation in energy of the electron-hole pair that is created or destroyed, respectively. For photon emission by electron-hole recombination, [9]

$$E_e - E_h = h\nu. \tag{3.12}$$

Momentum conservation also holds in photon interactions with holes and electrons. Simply put, the photon momentum must correspond to the difference in momenta of the recombined electrons (p_e) and holes (p_h)

$$p_e - p_h = \frac{h\nu}{c}. \tag{3.13}$$

The momentum conservation statement can be rewritten in terms of the electron and hole wave-vectors, k_e and k_h, respectively, as

$$k_e - k_h = \frac{2\pi}{\lambda}. \tag{3.14}$$

The magnitude of the photon momentum $\frac{h\nu}{c} = \frac{h}{\lambda}$ is far less than the range of momenta that electrons and holes can have; k_e and k_h reach a maximum at the first Brouillin zone, where k_e or $k_h = \frac{2\pi}{a}$. Since the lattice constant a of semiconductors is far smaller than the wavelengths of radiation whose energies match the semiconductor energy transitions, we can assume that $\frac{2\pi}{a} \gg \frac{2\pi}{\lambda}$. Using this inequality, the right hand side of Eq. 3.14 is approximately zero, yielding the selection rule for wave-vector [9]

$$k_e \approx k_h \equiv k. \tag{3.15}$$

The interpretation of Eq. 3.15 is this: only direct band-gap seimconductors are desirable for applications such as laser diodes, in which electron-hole pairs must combine radiatively. When the wave-vector of the electron in the conduction-band matches that of the hole in the conduction-band, recombination occurs through radiation emission. When the wave-vectors are mismatched, energy conservation still holds during recombination, resulting in the formation of a phonon. Energy released in the form of a photon is dissipated as vibrations and heat in the solid.

The relationship between E and k of the holes and electrons with which the photon interacts can be represented by the parabolic band approximation (Eqs. 3.6 and 3.7 and Fig. 3.1). The statement of energy conservation (Eq. 3.12) becomes

$$E_e - E_h = \left(\frac{\hbar^2 k^2}{2m_e^*} + E_g\right) - \left(-\frac{\hbar^2 k^2}{2m_h^*}\right) = h\nu,$$

from which we can solve for k^2

$$k^2 = \frac{2}{\hbar^2}\left(\frac{m_e^* m_h^*}{m_e^* + m_h^*}\right)(h\nu - E_G).$$

This formulation allows us to rewrite the energies for the electron and hole states

involved in absorption or emission by using Eqs. 3.6 and 3.7

$$E_e = E_C + \frac{m_e^*}{m_e^* + m_h^*}(h\nu - E_G) \tag{3.16}$$

$$E_h = E_V - \frac{m_e^*}{m_e^* + m_h^*}(h\nu - E_G). \tag{3.17}$$

Given that energy and momentum conservation hold, a photon interacts with a certain density of states, found by counting the number of states per unit photon frequency per unit volume of solid. Since this quantity incorporates both the conduction and valence density of states, it is called the optical joint density of states $D(\nu)$. [9] Equation 3.16 shows that a given conduction-band energy corresponds to a photon of a single frequency. Therefore, the number of photon states in an infinitesimal frequency range $D(\nu)d\nu$ is equal to the number of electron states in an infinitesimal range of conduction electron energies $D_e(E_e)dE_e$. Hence, $D(\nu) = \frac{dE_e}{d\nu}D_e(E_e)$. Taking the derivative of E_e with respect to ν and using Eq. A.1 to find $D_e(E_e)$,

$$D(\nu) = \left(2\frac{m_e^* m_h^*}{m_e^* + m_h^*}\right)\frac{(h\nu - E_G)}{\pi\hbar^2}. \tag{3.18}$$

An electron-hole pair will only be created if the incident photon energy is greater than or equal to the band-gap energy, so that the quantity $(h\nu - E_G) > 0$.

Let us consider the existence of an electron-hole pair in a semiconductor at thermal equilibrium. In this case, the Fermi level lies well within the band-gap ($k_B T \ll |E - E_F|$) and the electron and hole occupation probabilities can be approximated by the Fermi-Dirac distribution in Eqs. A.3 and A.5, respectively. For a photon to be emitted by recombination, there must first be an electron-hole pair in existence. In other words, an electron must have energy E_2 in the conduction-band such that $E_2 \geq E_V + E_G$ and a hole must have energy E_1 in the conduction band such that $(E_1 \leq E_V)$. Multiplying the probabilities of these two independent events gives the

probability of emission

$$p_{em}(\nu) = [f(E_2)]\,[1 - f(E_1)]\,. \tag{3.19}$$

In the same semiconductor, we can find the probability that a photon is absorbed. For this to occur, a hole must have some energy E_2 in the conduction-band, with probability $1 - f(E_2)$. An electron must also have an energy E_1 in the valence-band, which occurs with probability $f(E_1)$. The product of these two probabilities is the probability of absorption

$$p_{ab}(\nu) = [1 - f(E_2)]\,[f(E_1)]\,. \tag{3.20}$$

Dividing Eq. 3.19 by Eq. 3.20 yields

$$\frac{p_{em}}{p_{ab}} = \exp\left[\frac{E_1 - E_2}{k_B T}\right]. \tag{3.21}$$

Because E_1 is a valence-band energy and E_2 is a conduction-band energy, the exponent is negative, and the probability of emission is less than the probability of absorption, $p_{em} < p_{ab}$. Therefore, for a semiconductor in thermal equilibrium, stimulated emission can't occur.

Now, let us consider a semiconductor in quasi-equilibrium, with separate Fermi levels for the electrons and holes, E_{F_e} and E_{F_h}, respectively. We further assume that $E_{F_e} > E_{F_h}$. In a similar manner to the case of a semiconductor in thermal equilibrium, we can write down the probabilities of emission and absorption. The difference here is that the holes and electrons now have separate Fermi levels. Thus the requirements for emission and absorption are the same as before

$$p_{em}(\nu) = [f_e(E_2)]\,[1 - f_h(E_1)]\,, \tag{3.22}$$

$$p_{ab}(\nu) = [1 - f_e(E_2)]\,[f_h(E_1)]\,, \tag{3.23}$$

but with the separate Fermi-Dirac distributions for the holes and electrons

$$f_e(E) \equiv \frac{1}{1+\exp\left[\frac{E-E_{F_e}}{k_BT}\right]}, \tag{3.24}$$

$$f_h(E) \equiv \frac{1}{1+\exp\left[\frac{E-E_{F_h}}{k_BT}\right]}. \tag{3.25}$$

We find that the ratio of emission to absorption probabilities is

$$\frac{p_{em}}{p_{abs}} = \exp\left[\frac{(E_{F_e}-E_{F_h})-(E_2-E_1)}{k_BT}\right]. \tag{3.26}$$

In order for the probability of emission to exceed that of absorption, the difference in Fermi levels must exceed the difference in energy levels: $(E_{F_e}-E_{F_h}) > (E_2-E_1)$. In other words, the Fermi level for electrons must be farther above the conduction-band edge than E_2 and the Fermi level for holes must be farther below the valence-band edge than E_1. This is called the population inversion condition. Once the Fermi level for electrons has been raised high enough into the conduction-band and that for holes has been lowered far enough into the valence-band, stimulated emission is probabilistically favorable in the semiconductor medium.

When an electron-hole pair has been created, a photon can be released with probability p_{em} (Eq. 3.22). In deriving a description of the gain in a semiconductor medium, it is useful to know, for a unit volume of the solid, the time rate of spontaneous release of photons of a given frequency (photons per time per frequency per volume), denoted r_{sp}. Since the joint optical density of states (Eq. 3.18) describes the density of frequency states of an interacting photon, we divide $D(\nu)$ by the time it takes for recombination to occur. Hence

$$r_{sp}(\nu) = \frac{1}{\tau_r} D(\nu) p_{em}(\nu), \tag{3.27}$$

in which we call τ_r the recombination lifetime of an electron-hole pair.

When an electron hole pair has been created and photons are incident upon the solid, stimulated emission can occur. The radiation incident upon the solid is quantified as a photon-flux spectral density ϕ_ν (photons per area per time per unit frequency interval). When radiation is emitted, it interacts with a characteristic cross section of the solid given by [9]

$$A(\nu) \equiv \frac{\lambda^2}{8\pi\tau_r} g(\nu), \tag{3.28}$$

where $g(\nu)$ is the lineshape function, measuring the spectral distribution of emitted photons with wavelength λ. The rate of stimulated emission is then

$$r_{em}(\nu) = \phi_\nu \frac{\lambda^2}{8\pi\tau_r} D(\nu) p_{em}(\nu). \tag{3.29}$$

The quantity $r_{em}(\nu)$ is the number of photons emitted per time per frequency per volume in the solid, which we shall refer to as the stimulated emission rate. Equation 3.29 shows that increasing the number of photons incident on a unit area per unit time per unit frequency interval of the solid, ϕ_ν, results in a proportional increase in emission rate. Similarly, it seems sensible that, for a shorter pair-recombination lifetime τ_r, the rate of emission is higher. By the same logic, the rate of absorption r_{ab} is

$$r_{ab}(\nu) = \phi_\nu \frac{\lambda^2}{8\pi\tau_r} D(\nu) p_{ab}(\nu). \tag{3.30}$$

The net rate of radiation gain is thus given by the difference between absorption and emission rates $|r_{em}(\nu) - r_{ab}(\nu)|$.

Finally, we are in a position to express the gain coefficient in a semiconductor and identify the conditions under which lasing occurs. A useful conceptualization in the discussion of laser diodes is to picture a section of semiconductor material with unit end area, as in Fig. 3.2. In the active region of a diode laser, a photon-flux spectral density $\phi_\nu(x)$ is incident upon a cross-sectional area at position x. An infinitesimal

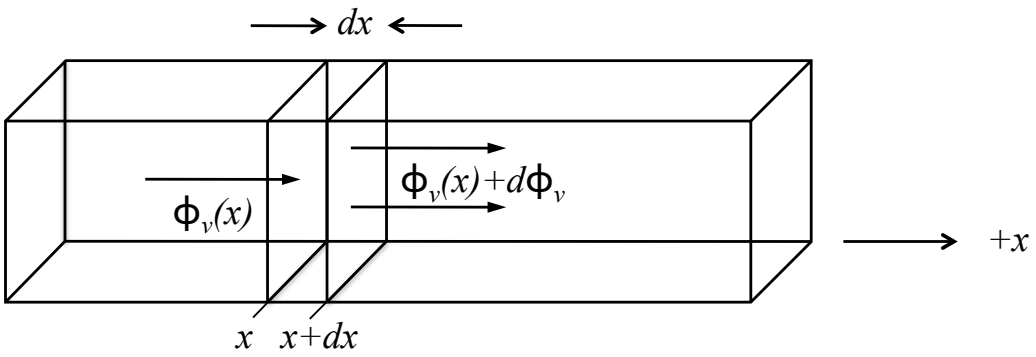

Figure 3.2: Conceptualization of gain in semiconductor media.

distance dx into the solid, at $x + dx$, photons with spectral flux density $\phi_\nu(x) + d\phi_\nu$ travel through the solid. To find the number of photons per time per unity frequency interval incident on the cross sectional area, we multiply by the net rate of radiation gain, or $[r_{em}(\nu) - r_{ab}(\nu)]\, dx$. Now, we can quantify the change in photon spectral flux density through an infinitesimal thickness of the semiconductor:

$$\frac{d\phi_\nu(x)}{dx} = \frac{\lambda^2}{8\pi\tau_r} D(\nu) \left[r_{em}(\nu) - r_{ab}(\nu)\right] \equiv \gamma_\nu \phi_\nu(x). \tag{3.31}$$

Substituting in Eqs. 3.29 and 3.30 into Eq. 3.31 yields an expression for the gain coefficient γ_ν

$$\gamma_\nu = \frac{\lambda^2}{8\pi\tau_r} D(\nu) \left[p_{em}(\nu) - p_{ab}(\nu)\right]. \tag{3.32}$$

We see that the rate of emission of photons must exceed the rate of absorption (Eq. 3.31) or, alternately, the probability of emission must be greater than that of absorption (Eq. 3.32) in order for the gain coefficient to be greater than zero. With a gain coefficient greater than zero, light amplification can occur by the stimulated emission of radiation.

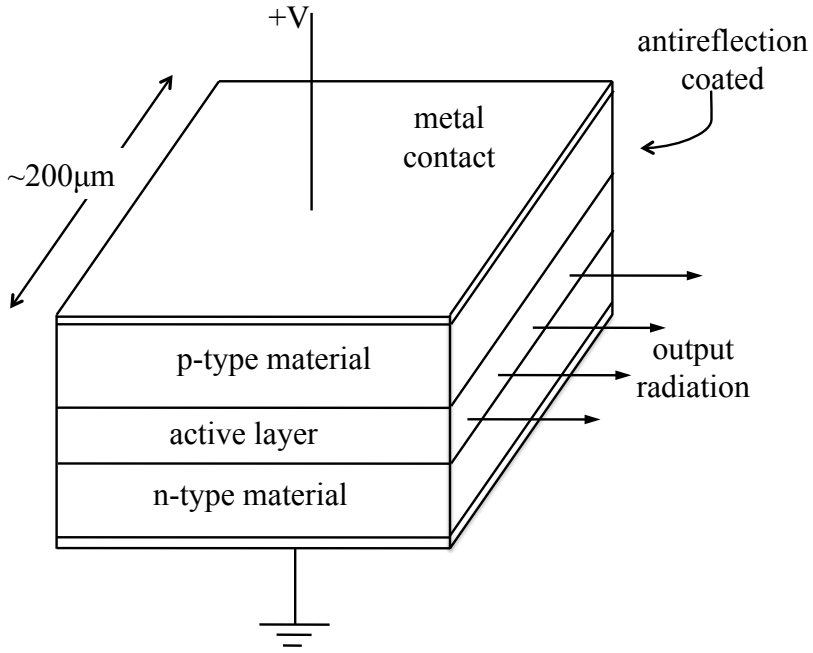

Figure 3.3: Diagram of the Littman TEC 500 laser diode, adapted from source [2].

3.2.2 Diode Lasers

Diode lasers are essentially composed of two components: a laser diode chip and an external lasing cavity. The diode chip shown in Fig. 3.3 consists of an intrinsic semiconductor layer flanked by a p-type and n-type layer, called a p-i-n junction. Because the depletion layer can extend deep into either side of a junction, the depletion layer of the p-i junction and that of the i-n junction are such that the depletion layer encompasses the entire intrinsic layer.[9] Electrons are injected into the n-type layer by sending an injection current through it, also known as a photodiode current i_{pd}. This creates electron-hole pairs in the junction which then recombine via stimulated and spontaneous radiative emission in the intrinsic layer, giving the intrinsic layer the name "active layer." The minimum current required for light to be emitted from the photodiode is known as the threshold current i_{th}. Above threshold, the output radiation power is proportional to the difference between photodiode current and threshold current.

The radiation emitted from the laser diode then enters the external lasing cavity.

The external cavity consists of a mirror and a diffraction grating. The diffraction grating sends the zeroth diffraction order out of a hole in the front plate of the laser chasis, where it serves as the laser output. The first diffraction order is reflected back into the external cavity. The external cavity permits a standing wave mode of oscillation with wavelength given by $\lambda = \frac{2l}{m}$, where $m = 0, 1, 2 \ldots$ and l is the cavity-length. Thus, by changing the length of this cavity, we can change the wavelength of the laser output beam. Because the cavity can support multiple modes, the laser often emits radiation at more than one peak wavelength. The spacing between these peaks is given by

$$\Delta\nu = \frac{c}{2nl}, \tag{3.33}$$

where l is the length of the cavity and n is the index of refraction of the material in the cavity. This effect arises when tuning the laser used in this project.

3.2.3 The Littman Laser TEC 500

Throughout this project, we use a Littman configuration Sacher model TEC 500 diode laser with an output of 780 nm. We chose this laser for its high optical output power of up to 150 mW, its narrow linewidth, the wavelength's proximity to the 780.24 nm ^{85}Rb emission line, its wavelength tuning capabilities, and because Jeff Dunham gave it to us. Because the scope of this project includes understanding the function of a diode laser, the basic tuning characteristics of the TEC 500 are discussed here.[4]

Figure 3.4 is a labeled photograph of the TEC 500. The diode chip in the TEC 500 is approximately 200 nm in length. The end of the chip from which radiation is released has been antireflection coated to reduce reflectivity by a factor of 10^3, thereby increasing the power of radiation emitted from the laser diode. [11] The radiation then enters the external cavity, which is made up of a reflective diffraction grating

[4] A comprehensive study of the tuning characteristics of diode lasers is not one of the goals of this project. Previous thesis students, such as Bonner (1992), have conducted such studies. [10]

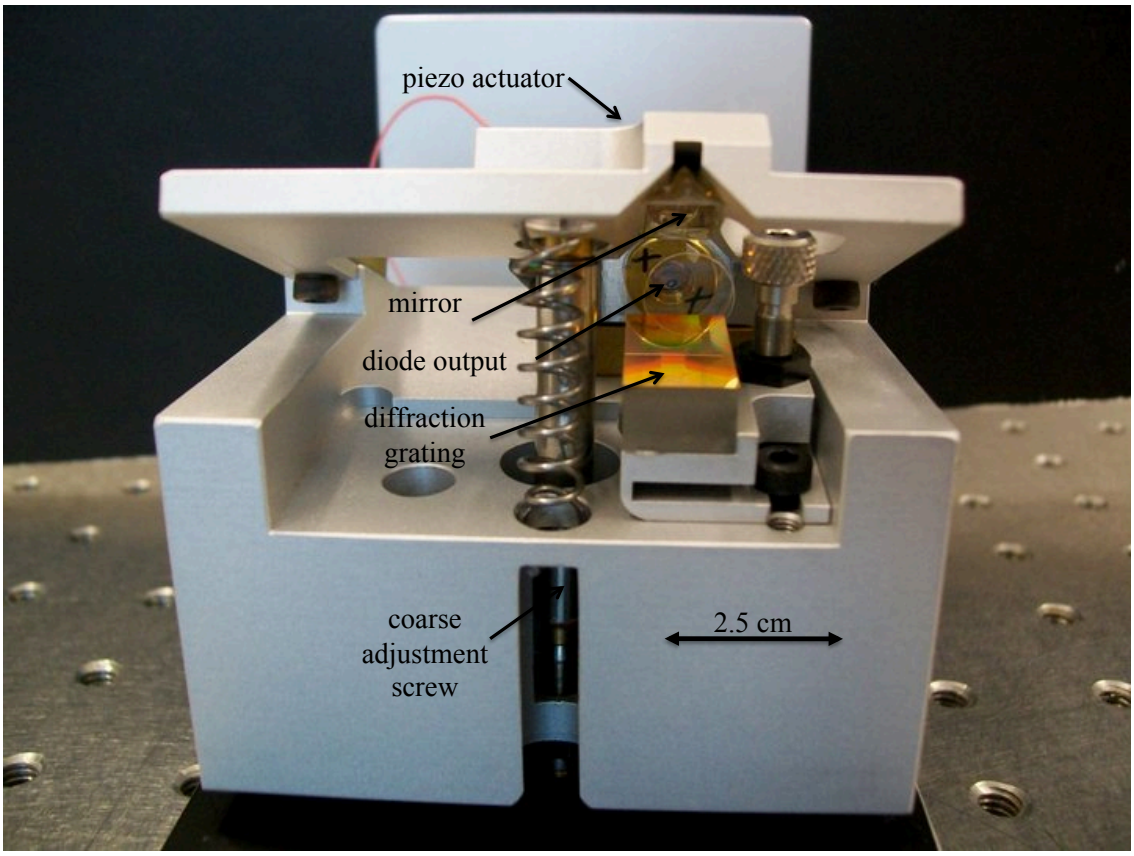

Figure 3.4: Photograph of the Sacher TEC 500 laser diode and external cavity. The external chassis has been removed to reveal these components.

and a mirror.

The position of the mirror in the TEC 500 can be adjusted in order to alter the length of the cavity and change the modes that the cavity supports. Coarse adjustments of the mirror position in the TEC 500 can be made by turning an adjustment screw located on the underside of the laser chassis, allowing for up to 30 nm of coarse wavelength tunability. While the manufacturer, Sacher, claims that the wavelength can be adjusted by 6 nm with one full turn of the coarse adjustment screw, we found that a full turn results in approximately 4.4 ± 0.1 nm change in wavelength.[11] Turning the screw counterclockwise when viewed from the top of the chassis decreases the wavelength, while turning the screw clockwise increases the output wavelength.

We can make fine cavity-length adjustments by applying a voltage to a piezoelec-

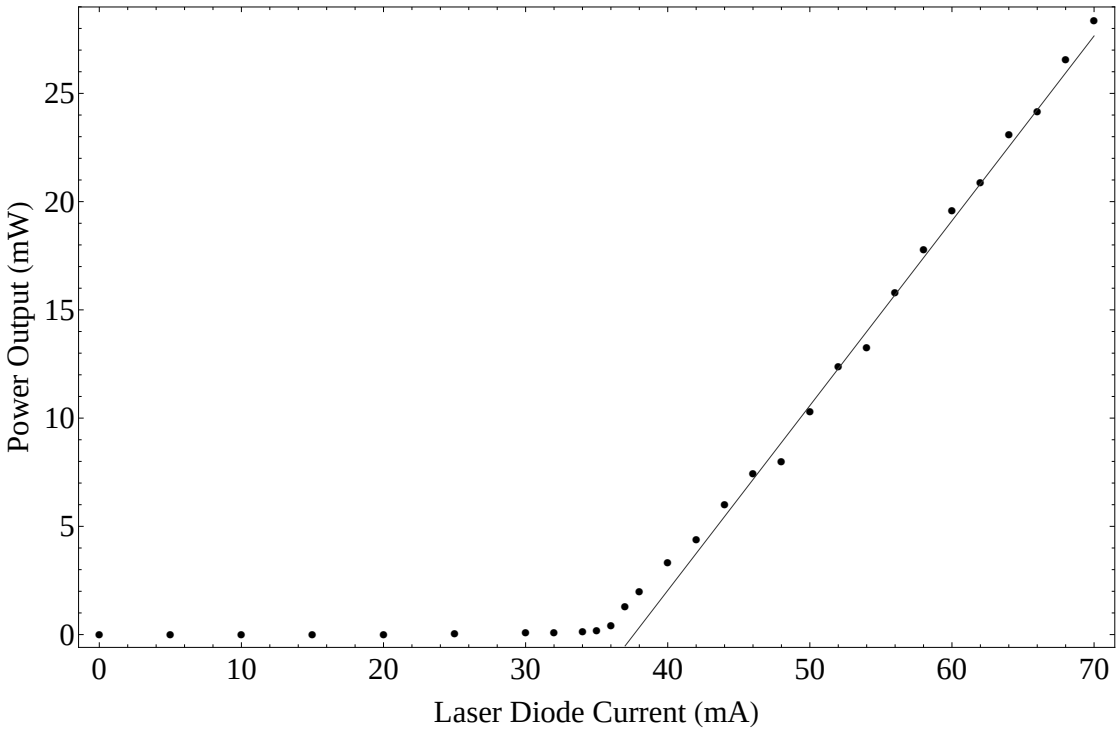

Figure 3.5: Power as a function of laser diode current for the TEC 500 laser. The solid line is a linear fit to data points above the threshold current.

tric actuator, allowing for adjustments of ~ 0.60 nm.[11] We measured a change in wavelength of about 0.1 nm for a change in piezo voltage of 20 V. This was in fairly good agreement with the manufacturer's claim of a 0.60 nm change in wavelength produced by a 100 V change in piezo voltage. The piezo voltage can be controlled by computer, an external ramp signal, or manually; we will revisit these controls when discussing our spectroscopy experimental setup in Chapter 5.

In studying the output power of the TEC 500 as a function of photodiode current i_{pd}, we found that there was a current threshold below which no lasing occurred and above which the output power increased approximately linearly with photodiode current. The topics discussed thus far in this chapter should lead us to expect this result; the energy of the Fermi level depends upon electron concentration and the Fermi level for electrons must be raised into the conduction-band for population inversion to occur. As shown in Fig. 3.5, the observed threshold current was about

37 mA, as opposed to the manufacturer's stated value of 28 mA at 780 nm.[11] Changing the photodiode current also led to a change in the output wavelength. This is because the injection current causes joule heating in the diode chip, which leads to thermal expansion. The laser often displayed multi-mode behavior, as discussed in the previous section. Figure 3.6 superimposes four spectra of the TEC 500 output to show how the output transitions between single-mode and multi-mode operation as the photodiode current changes. We will see in Chapter 5 that jumps between modes are manifested as discontinuities in absorption spectra, an undesirable feature when probing atomic structure.

Increasing the operating temperature of the TEC 500 results in thermal expansion of the diode chip and of the components that make up the external cavity, resulting in a decrease in the output wavelength. Since thermal expansion is linear for the small temperature changes in the acceptable operating temperature (22° C), the change in output wavelength is also expected to be linear with temperature.[11][12] We found that the laser was likely to mode-hop at certain temperatures and determined that setting the laser diode temperature control to 20° C allowed us to tune the laser frequency without observing mode-hopping. An understanding of these tuning characteristics enables us to find satisfactory laser operation settings for use in obtaining absorption spectra and to stabilize the laser output in the future.

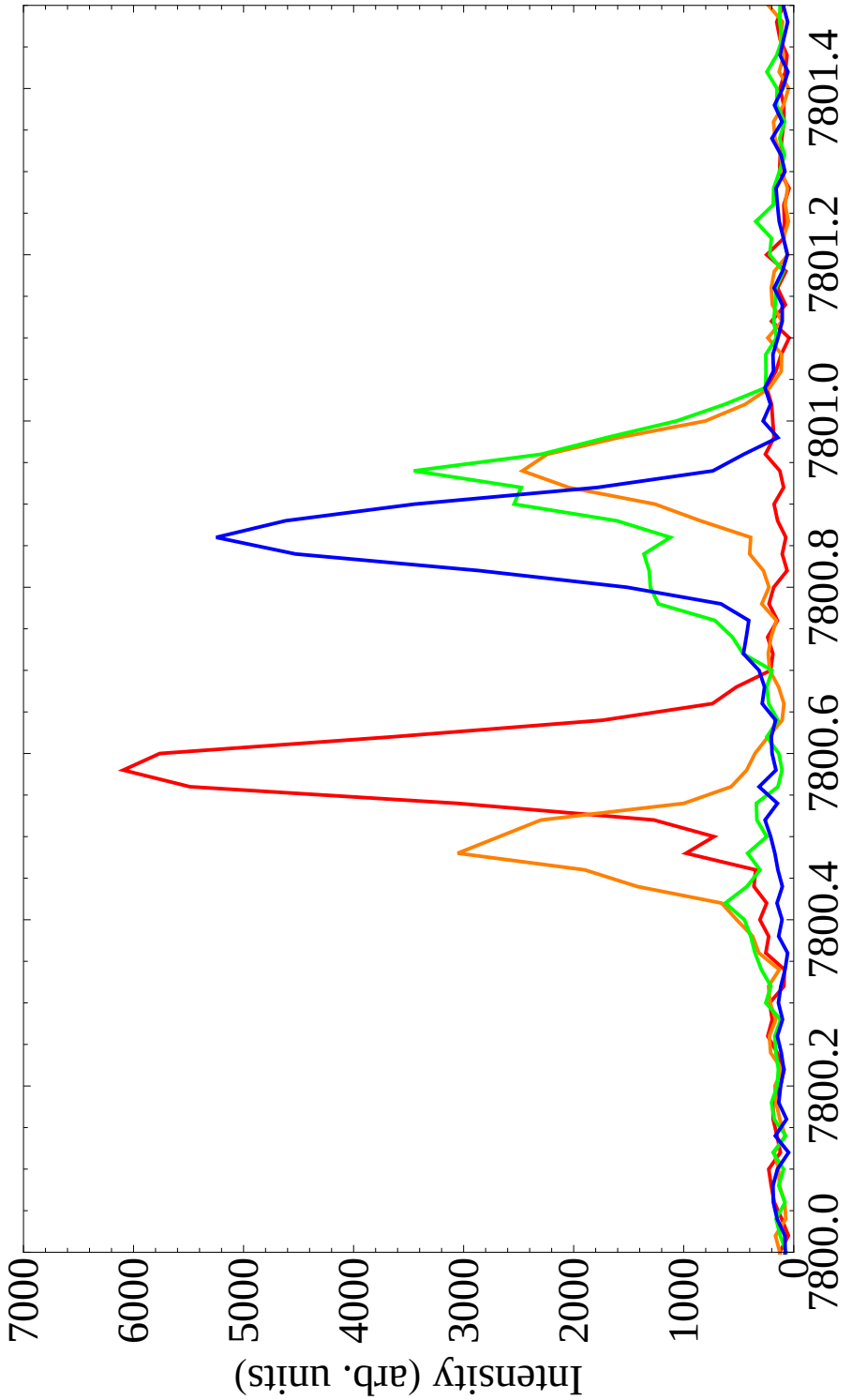

Figure 3.6: Spectra of the TEC 500 output as photodiode current i_{pd} is changed from 71.0 mA (red), to 66.0 mA (orange), to 64.0 mA (green), to 62.0 mA (blue) at a constant temperature of 22.5° C. Two lasing modes were observed. The orange spectrum shows simultaneous lasing in both modes, the green shows the transition to single-mode lasing, and the red and blue spectra show single-mode lasing. The spectra were taken with a SPEX 1704 grating spectrometer.

Chapter 4

Absorption Spectroscopy

Now that we understand how the diode laser output frequency changes as a function of laser current and temperature, we must match the output wavelength to an atomic transition in ^{85}Rb. To do this, we obtain absorption spectra of ^{85}Rb which will be used in future experiments to obtain a feedback signal for laser stabilization. This chapter investigates the structure of the atom, how atomic transitions arise, and the theory behind absorption spectroscopy techniques.

4.1 Atomic Structure

In 1913, Danish physicist Niels Bohr proposed an atomic model for which a single electron orbits a positively charged nucleus at discrete radaii, thus producing a discrete set of allowed energy levels for electrons. While classical mechanics predicted that electrons could take on any energy, Bohr postulated that electrons occupied discrete energy levels given by [1]

$$E_N = -1/2\alpha^2 Z^2 \mu c^2 \frac{1}{N^2}, \tag{4.1}$$

[1] This is the same result that is obtained from the time-independent Schrödinger equation. When separated in spherical coordinates, the radial component yields these values for energy levels, while the angular component gives the spherical harmonics.

where μ is the effective mass of the electron-nucleus system, α is the fine structure constant,

$$\mu \equiv \frac{m_e m_n}{m_e + m_n}, \;\; \alpha \equiv \frac{e^2}{4\pi\epsilon_0 \hbar c} \approx \frac{1}{137}$$

N is a non negative integer (called the principal quantum number), m_e is the mass of an electron, m_n is the mass of the nucleus, and e is the charge of the electron. [13] In his model, the electron has orbital angular momentum that is quantized in integer values of $\hbar$, $\left|\vec{L}\right| = N\hbar$. Bohr also said that when the electron changes to a lower or higher energy level, it does so by emitting or absorbing a photon of energy equal to the energy difference between the initial and final orbits. Bohr's model was acclaimed for its agreement with the emission spectrum of hydrogen predicted by the Rydberg equation.[2]

In spite of its early success, the Bohr model was far from complete. First, we will consider the angular momentum of the electron as it orbits the positively charged nucleus due to the attractive Coulomb interaction. This is known as the orbital angular momentum, denoted $\vec{L}$. Second, we consider the electron's angular momentum of rotation about its axis, called the intrinsic angular momentum or spin $\vec{S}$. These two angular momenta couple to make the total electron angular momentum $\vec{J}$, further affecting the energy levels. Third, we will consider the nucleus' total angular momentum, simply called the nuclear angular momentum $\vec{I}$. [15] [16]

The time-independent Schrödinger equation for an electron in an atom gives the quantum number L associated with the orbital angular momentum of the electron. The orbital angular momentum quantum number L can take on the values $\{L = 0, 1, \ldots N-2, N-1\}$. Given in terms of the orbital angular momentum quantum

[2]The Rydberg equation says that $\frac{1}{\lambda} = R\left(\frac{1}{N_i^2} - \frac{1}{N_f^2}\right)$, where R is the Rydberg constant, N_i and N_f are the initial and final principal quantum numbers, respectively. [14]

number, the magnitude of the angular momentum is [15]

$$\left|\vec{L}\right| = \sqrt{L(L+1)}\hbar. \tag{4.2}$$

Taking a z-axis that is perpendicular to the plane of electron orbit, the projection of $\vec{L}$ onto the z-axis is $L_z = m_L\hbar$, where the quantum number m_L takes on $2L+1$ values, $m_L = \{-L, -L+1, \ldots, L-1, L\}$. Since the electron has negative electric charge, there is a magnetic dipole moment associated with its orbit, given by [16]

$$\vec{\mu}_L = \frac{-g_L\mu_B\vec{L}}{\hbar}. \tag{4.3}$$

In the second equality, g_L is known as the orbital g-factor, and

$$\mu_B \equiv \frac{e\hbar}{2m_e} = 9.27 \times 10^{-24}\frac{\mathrm{J}}{\mathrm{T}} \tag{4.4}$$

is the Bohr magneton, the customary unit for atomic magnetic moments.[15] The angular momentum quantum numbers are often assigned letter values, with $\{s, p, d, f, g \ldots\}$ corresponding to $L = \{0, 1, 2 \ldots\}$.

The electron also has an intrinsic angular momentum $\vec{S}$, also known as "spin." The projection of $\vec{S}$ onto the z-axis is $S_z = m_S\hbar = \pm\frac{1}{2}\hbar$, known as "spin up" and "spin down," respectively. The quantum number associated with spin has only one value, $S = \frac{1}{2}$. Similar to the orbital angular momentum, intrinsic angular momentum takes on values $\left|\vec{S}\right| = \sqrt{S(S+1)}\hbar$. The electron has intrinsic magnetic moment [15]

$$\vec{\mu}_S = -\frac{g_S\mu_B}{\hbar}\vec{S}, \tag{4.5}$$

where g_S is the intrinsic g-factor.[16] Since the orbiting electron produces a magnetic field (similar to a loop of wire), there is an interaction between the intrinsic and orbital

angular momenta, known as spin-orbit (L-S) coupling, that results in a shift in the energy levels of Eq. 4.1. This energy shift is given by $\Delta E = -\vec{\mu_S} \cdot \vec{B_L}$, where $\vec{B_L}$ is the magnetic field due to the electron orbit, which is somewhat like a current loop. To describe the L-S coupling we say that the electron has total angular momentum given by $\vec{J} = \vec{L} + \vec{S}$, with quantum numbers given by $J = \{|L-S|, |L-S+1|, \ldots, L+S-1, L+S\}$.[15] The total electron angular momentum takes on quantized values $\left|\vec{J}\right| = \sqrt{J(J+1)}\hbar$ and its projection onto the z-axis is $J_z = m_J\hbar$. The quantum number m_J takes on $2J+1$ values: $m_J = \{-J, -J+1, \ldots, J-1, J\}$. Accounting for both magnetic moment contributions, the total atomic magnetic moment is

$$\vec{\mu}_J = \vec{\mu}_S + \vec{\mu}_J. \tag{4.6}$$

The atomic structure arising from the spin-orbit interaction is known as fine structure.

Finally, we must account for the fact that the nucleus has an intrinsic angular momentum, referred to as nuclear spin. It may be apparent by now that the nuclear spin will couple with the total electron angular momentum, resulting in further splitting into non-degenerate energy levels. The total atomic angular momentum, then, is $\vec{F} = \vec{I} + \vec{J}$. The total atomic angular momentum quantum number can have value $F = \{|I-J|, |I-J+1|, \ldots, I+J-1, I+J\}$ and its projection onto the z-axis (again, perpendicular to the plane of electron orbit) is $m_F = \{-F, -F+1, \ldots, F-1, F\}$. In the absence of any external magnetic field, the energy levels associated with each m_F for a given F are degenerate. The atomic structure associated with the total atomic angular momentum is produced by an $\vec{I} \cdot \vec{J}$ interaction that is similar to the $\vec{L} \cdot \vec{S}$ interaction and is referred to as hyperfine structure. ^{85}Rb has $I = \frac{5}{2}$ and ^{87}Rb has $I = \frac{3}{2}$.[17] Therefore, for the $5P_{3/2}$ electronic ground state in ^{85}Rb, the total atomic angular momentum takes on values $F = \{1, 2, 3, 4\}$, for example.

As an alkali metal ^{85}Rb has one valence electron that absorbs and emits radiation in the $5S_{1/2} \rightarrow 5P_{3/2}$, known as its optically active electron. Figure 4.1 is an energy-level diagram for ^{85}Rb, showing the $F = 3$ hyperfine ground state to $F' = 4$ transition that is used as the trapping transition in laser cooling. The goal of the atomic spectroscopy studies is to match the laser output to this atomic transition.

All of the atomic structure discussed so far assumes the absence of an external magnetic field. In 1896, Pieter Zeeman observed that, when an atom is placed in an external magnetic field, a given spectral emission line splits into several lines. In recognition of his observation, this effect is named the Zeeman effect. In the case that the external magnetic field $\vec{B}_{ext}$ is weak compared to the magnetic field due to the orbital angular momentum of the electron (i.e. $\vec{B}_{ext} < 1$Tesla), the atom obeys L-S coupling. In other words, the external magnetic field is not strong enough to overcome the electron spin-orbit interaction. For an atom with total electron magnetic moment $\vec{\mu}_J$, the atom will have potential energy due to its orientation in the external magnetic field

$$\Delta E = -\vec{\mu}_J \cdot \vec{B}_{ext}. \text{ [15]} \tag{4.7}$$

Equation 4.2 tells us that the atom only takes on discrete orientations in space. This implies that the energy splitting described in Eq. 4.7 is quantized, with one energy corresponding to each orientation of the atom in the external magnetic field. This is known as Zeeman splitting.

At the hyperfine structure level, the potential energy due to the orientation of the atom's total magnetic moment in the external magnetic field lifts the degeneracy on the energy levels with quantum number m_F. The magnitude of the Zeeman splitting is given by

$$\Delta E = \mu_B B_{ext} g_F m_F, \tag{4.8}$$

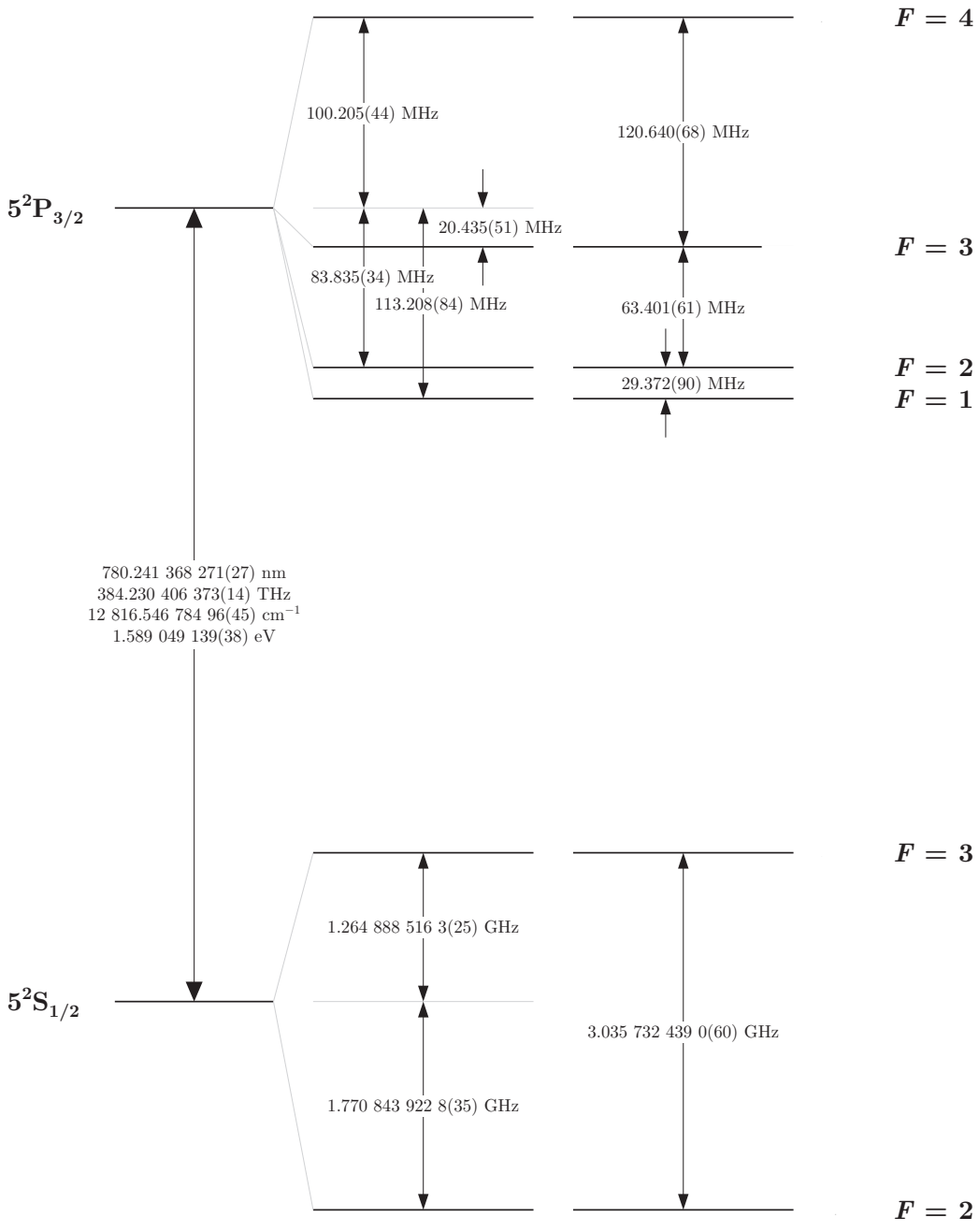

Figure 4.1: Energy level diagram for ^{85}Rb. After ref. [18].

where g_F is the Landé g_F-factor.[3] [15][16] Equation 4.8 indicates that the energy levels split into $2F+1$ discrete values, one for each value of m_F. In other words, each projection of $\vec{F}$ onto an axis parallel to the external magnetic field has a Zeeman shifted energy sub-level associated with it.

As an example, let us consider the $(F = 3 \rightarrow F' = 4)$ transition in ^{85}Rb. The $F = 3$ ground state splits into 7 non-degenerate energy levels with total magnetic moment quantum number $m_F = \{\pm 3, \pm 2, \pm 1, 0\}$. The $F' = 4$ excited state splits into 9 non-degenerate energy levels with total magnetic moment quantum number $m_F = \{\pm 4, \pm 3, \pm 2, \pm 1, 0\}$. The selection rules for atomic transitions at the hyperfine structure level necessitate that $\Delta m_F = 0, \pm 1$. [15] When undergoing a transition, angular momentum is conserved and the atom must gain or lose a quantum of angular momentum associated with the change in m_F. We will revisit this concept in Chapter 6.

4.2 Absorption and Dispersion

When white light shines on a prism the range of frequencies refract at different angles. This familiar phenomenon, called dispersion, occurs because the material's refractive index is frequency dependent. Consider monochromatic laser light matching an atomic resonance transition of a particular atom incident upon a gas of those atoms. The atoms absorb a fraction of the laser beam, but the rest passes through the gas. An absorption curve measures the fraction of the laser beam power that is absorbed as a function of laser wavelength. If atoms absorbed light only at their resonant frequency, a plot of absorption as a function of laser energy would have a dirac-delta function shape. Due to the frequency dependence of absorption, the absorption spectrum has a finite linewidth, the shape of which can be predicted with a classical model.

[3] The Landé g_F-factor can be found for a given transition in rubidium in ref. [18] or [19].

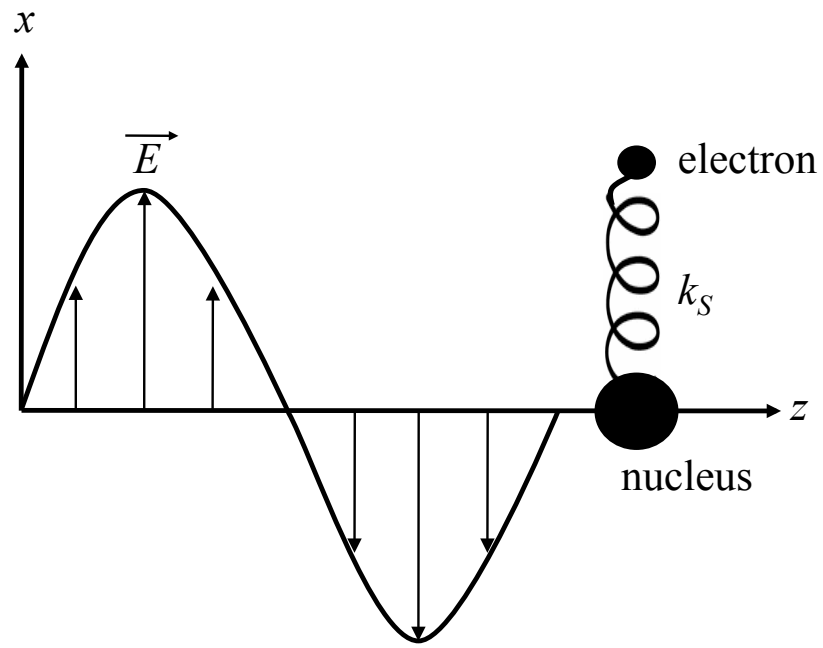

Figure 4.2: Schematic diagram of the Lorentz model for absorption. The force between the (stationary) nucleus and electron is modeled by a spring with spring constant k_S. The incident magnetic field $\vec{E}$ displaces the electron from its equilibrium position.[2] [3]

A dilute gas behaves as though each electron is bound to a specific atom, with negligible interaction between atoms. H.A. Lorentz proposed a model of the atom in which an electron is bound to a positively-charged nucleus by a force that can be modeled by a spring with spring constant k_s, as shown in Fig. 4.2. [2] Thus, the electron's potential energy in the absence of an electric field is $U(x) = \frac{1}{2}k_s x^2$, corresponding to a force $F(x) = -k_s x$ when the electron is displaced by a distance x from equilibrium. An electric charge in the presence of an electric field experiences a force. In the Lorentz model of absorption, the electron experiences the force of the time-varying electric field of an electromagnetic wave of angular frequency ω and maximum amplitude E_0:

$$\vec{F}_E = q\vec{E} = qE_0 cos(\omega t)\hat{x}. \tag{4.9}$$

Lorentz also assumed the presence of a damping force on the electron that was pro-

portional to the electron's velocity:

$$\vec{F}_{Damping} = -\gamma m_e \frac{d\vec{x}(t)}{dt}, \tag{4.10}$$

where $\vec{x}(t)$ is the electron position vector relative to the nucleus, m_e is the electron mass, and γ is the damping constant. The damping constant is the inverse of the excitation lifetime of the upper state of the radiative transition. [2] Equating all of the forces acting on the electron in this model, Newton's second law governs the motion of the electron:

$$m_e \frac{d^2x}{dt^2} = -k_s x - \gamma m_e \frac{dx}{dt} + qE_0 cos(\omega t). \tag{4.11}$$

This second order, linear differential equation describes a damped, driven simple harmonic oscillator. For a single-electron atom in which the electron oscillates at natural, undamped, undriven frequency $\omega_0 \equiv \sqrt{k_s/m_e}$, the equation of motion takes on the recognizable form:

$$\frac{d^2x}{dt^2} + \gamma \frac{dx}{dt} + \omega_0^2 x = \frac{q}{m_e} E_0 cos(\omega t). \tag{4.12}$$

This equation of motion for the electron leads to an expression for the absorption coefficient $a(\omega)$ of a gas that depends on frequency. While the details of the derivation have been deferred to Appendix B, it can be shown that for an atom such as rubidium with a single optically active electron, [3]

$$a(\omega) = \frac{Nq^2}{m_e \epsilon_0 c} \frac{2\delta\omega_0\omega^2}{(\omega_0^2 - \omega^2)^2 + (2\delta\omega_0)^2\omega^2} \tag{4.13}$$

where N is the number of Lorentz oscillators per unit volume of the gas and I have defined the quantity $\delta\omega_0 \equiv \gamma/2$. If the damping coefficient in the differential equation is far less than the natural frequency of oscillation, $\gamma \ll \omega_0$, then $\delta\omega_0$ is very nearly the half-width at half-maximum of the absorption curve.

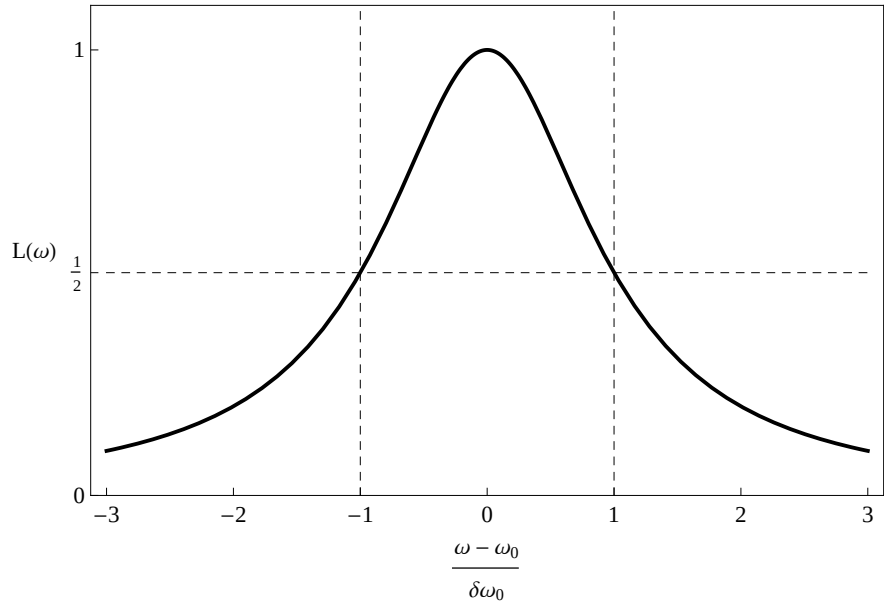

Figure 4.3: The Lorentzian lineshape function describes absorption of radiation with frequency close to that of the resonant transition.

If we are interested in the absorption near resonance, as is the case in absorption spectroscopy, then we can simplify the expression for the absorption coefficient. For a driving frequency ω near the natural frequency of oscillation ω_0, $|\omega_0 - \omega| \ll \omega, \omega_0$. We can use this to approximate the term

$$(\omega_0^2 - \omega^2)^2 = [(\omega_0 - \omega)(\omega_0 + \omega)]^2 \approx [(\omega_0 - \omega)(2\omega)]^2 .$$

In this approximation, the absorption coefficient takes the form

$$a(\omega) = \frac{Nq^2}{2m_e\epsilon_0 c}\frac{\delta\omega_0}{(\omega_0 - \omega)^2 + \delta\omega_0^2} \tag{4.14}$$

$$= \frac{Nq^2}{2m_e\epsilon_0 c}L(\omega). \tag{4.15}$$

The function $L(\omega)$ is known as the Lorentzian lineshape function

$$L(\omega) = \frac{\delta\omega_0}{(\omega_0 - \omega)^2 + \delta\omega_0^2}, \tag{4.16}$$

which is plotted in Fig. 4.3 for frequencies near resonance. Evaluating the Lorentzian at $\omega \pm \delta\omega_0$ makes it clear that $\delta\omega_0$ is the half-width at half-maximum (HWHM) of the Lorentzian. Thus, $2\delta\omega_0$ is known as the natural or Lorentzian linewidth of the absorption spectrum.

4.3 Doppler Broadening

The absorption spectra obtained experimentally typically have a far wider profile than that of the Lorentzian described above, because the spectrum is broadened by the Doppler effect. Atoms in a gas have a range of velocities given by the Maxwell-Boltzmann distribution. When laser light of wavevector $\vec{k}$ passes through a sample of gas, atoms moving in the direction opposite to $\vec{k}$ observe the frequency of radiation to be higher than the laser frequency in the lab frame. Conversely, for an atom moving in the same direction as $\vec{k}$, the observed frequency is less than the laser frequency in the lab frame. Atoms in motion will absorb radiation that does not match the resonance ω_0, resulting in a broader absorption spectrum. An atom that has a resonant transition of angular frequency ω_0 when it is at rest absorbs at

$$\omega_0' = \omega_0 \left(1 + \frac{v}{c}\right), \tag{4.17}$$

if it is moving at speed v in the direction of laser beam propagation, with velocity $v \ll c$. Similarly, an atom moving opposite the direction of propagation absorbs at

$$\omega_0' = \omega_0 \left(1 - \frac{v}{c}\right). \tag{4.18}$$

In general the Doppler-shift in angular frequency of a moving atom can be written

$$\omega_0' - \omega_0 = -\vec{k} \cdot \vec{v}, \tag{4.19}$$

which indicates that the Doppler-shift depends upon the direction of the atom's velocity with respect to an incident laser beam. Equations 4.17 and 4.18 show that every Doppler-shifted absorption frequency corresponds directly to a particular atom velocity and, therefore, the number of atoms with velocities between v and $v + dv$ is the same as the number of atoms that absorb between ω and $\omega + d\omega$. Thus, the Maxwell Boltzmann distribution for atoms of mass m_a can be written as [2]

$$df(v) = \sqrt{\frac{m_a}{2\pi k_B T}} \exp\left[-\frac{m_a v^2}{2k_B T}\right] dv \tag{4.20}$$

to describe the fraction of atoms absorbing between frequencies ω and $\omega + d\omega$.[4] Solving Eq. 4.18 for v and making the change of variable in Eq. 4.20,

$$df(\omega) = \sqrt{\frac{m_a}{2\pi k_B T}} \exp\left[\frac{-m_a c^2(\omega - \omega_0)^2}{2k_B T \omega_0^2}\right] \left(\frac{c}{\omega_0} d\omega\right). \tag{4.21}$$

As previously stated, absorption measures the fraction of atoms in a gas absorbing a particular frequency of light. Therefore, the absorption $S(\omega)$ at a given frequency is proportional to the fraction of atoms that absorb that frequency and can be written

$$S(\omega) \equiv \frac{c}{\omega}\frac{df}{d\omega} = \sqrt{\frac{m_a c^2}{2\pi k_B T \omega_0^2}} \exp\left[\frac{-m_a c^2(\omega - \omega_0)^2}{2k_B T \omega_0^2}\right]. \tag{4.22}$$

This expression for absorption due to the Doppler effect is known as the Doppler lineshape function. It is useful to define a value for the HWHM of the Doppler lineshape function

$$\delta\omega_D \equiv \frac{\omega_0}{c}\sqrt{\frac{2k_B T}{m_a} \ln 2}, \tag{4.23}$$

in terms of which Eq. 4.22 can be written

$$S(\omega) = \frac{1}{\delta\omega_D}\sqrt{\frac{\ln 2}{\pi}} \exp\left[\frac{-(\omega - \omega_0)^2 \ln 2}{\delta\omega_D^2}\right]. \tag{4.24}$$

[4]The Maxwell-Boltzmann distribution (Eq. 4.20) is normalized to 1.

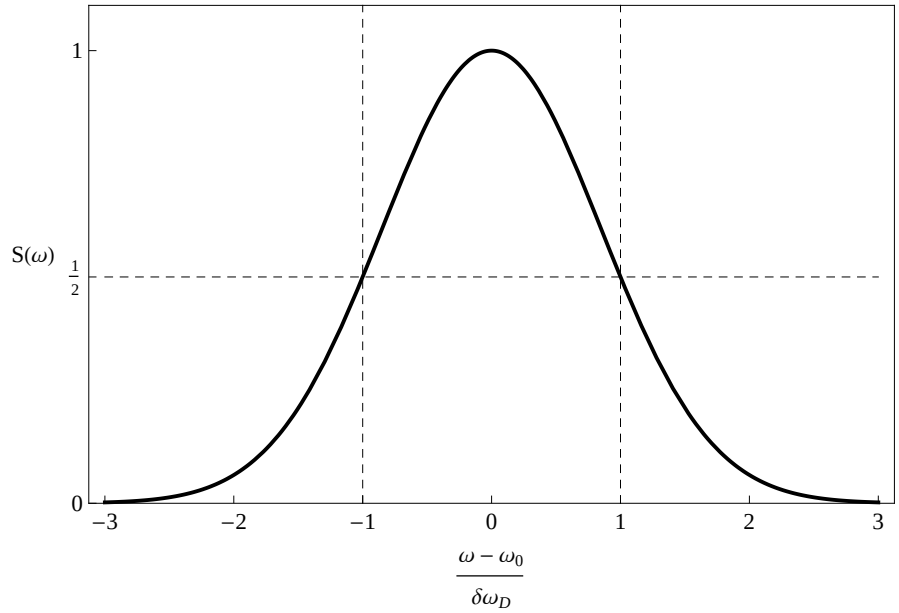

Figure 4.4: The Doppler lineshape function near resonance.

The Doppler-broadened linewidth for the $5S_{1/2}(F = 3, m_F = 3) \rightarrow 5P_{3/2}(F' = 4, m_{F'} = 4)$ transition in ^{85}Rb at 300 K is $2\delta\omega_D = 2\pi \cdot 259$ MHz [20], while the Lorentzian linewidth is $2\pi \cdot 5.98$ MHz.[5][22] The Doppler linewidth is greater than the spacing between hyperfine structure peaks in ^{85}Rb, as Fig. 4.1 shows. In order to view hyperfine structure, we must use methods that minimize the effects of Doppler-broadening in absorption spectra.

4.4 Saturated-absorption Doppler-Free Spectroscopy

In order to accurately determine the energies of the transitions that will be used in laser cooling, we must use a method to minimize the effects of Doppler broadening in our measurements of the rubidium spectrum. One such technique, called saturated-absorption spectroscopy, passes two laser beams through the gas sample, instead of one. The beams have the same frequency but different intensities. The higher

[5]Calculated from Eq. 4.23 using $\omega_0 = 2\pi \cdot 3.84 \times 10^{(14)}$Hz for the $5S_{1/2} \rightarrow 5P_{3/2}$ transition in ^{85}Rb and $m_a = 1.41 \times 10^{-25}$kg.[21]

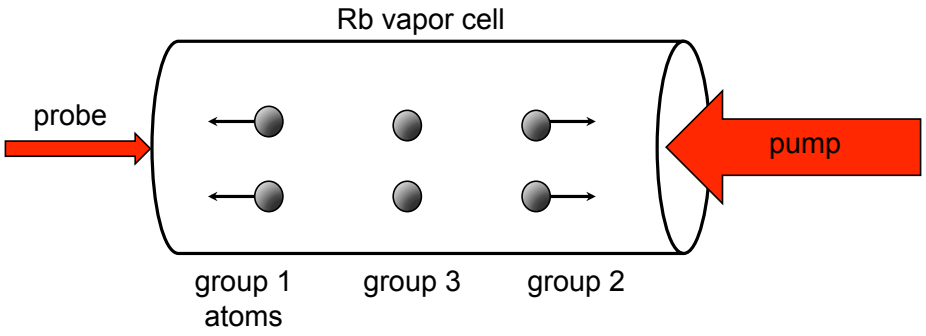

Figure 4.5: Schematic diagram illustrating the interaction of atoms with various velocities with the pump and probe beams. [13][23][21]

intensity beam is called the pump beam and the lower intensity beam is called the probe beam. As in normal fluorescence spectroscopy, the laser frequency is scanned over a range of frequencies about resonance.

Consider a gas, discussed previously, that contains atoms with velocity components both parallel and antiparallel to $\vec{k}$. In saturated-absorption spectroscopy, a very powerful beam called the pump beam is incident upon the gas, as shown in Fig. 4.5. This beam saturates absorption in the gas; of the population of atoms that observe this beam matching a resonant transition, only half can be in the excited state at a given time.

The key to Doppler-free spectroscopy is to make a weaker probe beam propagate through the gas in the direction opposite the pump beam, as shown in Fig. 4.5. To reveal the advantage of this configuration, let us picture the three groups of atoms shown in Fig. 4.5: those moving toward the probe beam (group 1), those moving toward the pump beam (group 2) and those that are stationary (group 3). When the laser is tuned far below or far above resonance, none of the atoms in the gas observe their resonant frequency and the gas is transparent to the particular frequency.

When the laser beam is tuned just below resonance ($\omega < \omega_0$), atoms absorb due to a blue-shift. Group 1 atoms observe the probe beam blue-shifted to match resonance and half of them are in the excited state. Group 1 atoms also see the pump beam

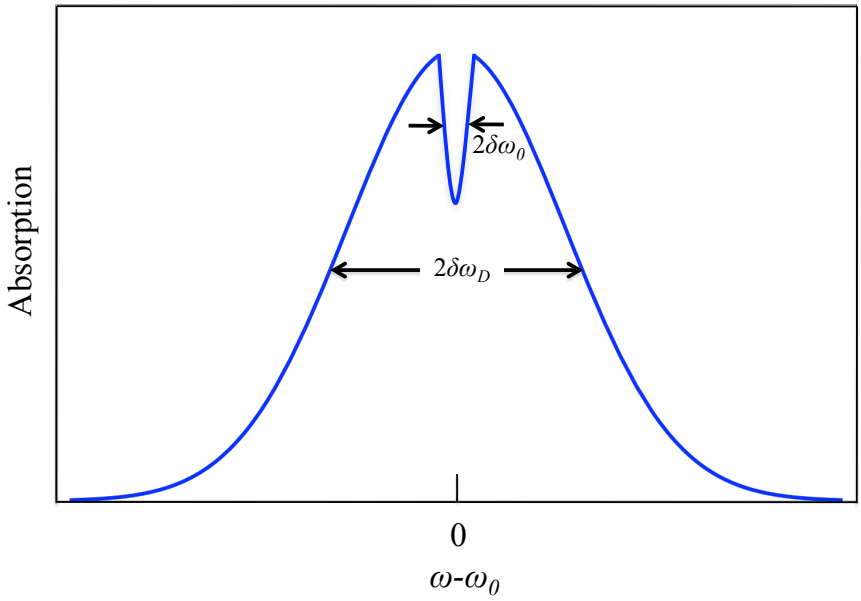

Figure 4.6: Idealized Doppler-free saturated-absorption spectrum. The saturated-absorption feature is centered about ω_0 and has the natural Lorentzian linewidth. [13][23][21]

red-shifted away from resonance and do not absorb from it. Group 2 atoms observe the pump beam blue-shifted to match resonance. Atoms at rest absorb from neither the pump beam nor the probe beam since the laser is off resonance.[13][21]

When the laser is tuned just above resonance ($\omega > \omega_0$), atoms absorb due to a red-shift. Group 1 atoms observe the pump beam red-shifted to resonance and absorb from it, while group 2 atoms observe the probe beam red-shifted to resonance. Again, atoms at rest do not absorb from either beam because the laser is off resonance.

If the laser is tuned to resonance ($\omega = \omega_0$), atoms at rest absorb the laser light. The group 3 atoms observe the resonant frequency from both the pump and probe beams. Since the pump beam is more intense, group 3 atoms have higher probabilities of absorbing from it than from the probe beam. Since only half of the group 3 atoms can be in the excited state, a smaller fraction of atoms will absorb the probe beam than in the off-resonance cases. Monitoring the intensity of the probe beam after it passes through the gas reveals a sharp decrease in absorption at exactly the resonant

frequency, as in Fig. 4.6. This feature pinpoints the frequency of an atomic transition, thereby minimizing the effects of Doppler broadening.

Chapter 5

Doppler-Free Spectroscopy Experiment and Results

5.1 The Stabilization Problem

In Chapter 3, we saw how parameters such as temperature, photodiode injection current, and cavity length affect the output of a diode laser. While tunability is a distinct advantage of diode lasers, environmental factors such as temperature changes and vibrations, as well as imperfections, such as drift in injection current or piezo-actuator voltage, can cause the laser output frequency to change. Such changes are undesirable in the laser cooling experiments that will be conducted, in which the laser must target the $5S_{1/2}(F = 3) \rightarrow 5P_{3/2}(F' = 4)$ cooling transition in ^{85}Rb, which has a natural linewidth of about 6 MHz.[18] In order to maintain a constant output frequency, a future project will be to set up an electronic stabilization system.

The stabilization system requires feedback about the frequency that the laser outputs. The simple Doppler-broadened absorption spectra discussed in the previous chapter do not meet these needs, as Doppler-broadening typically obscures hyperfine structure. Since we must lock the laser output to match the $5S_{1/2}(F = 3) \rightarrow$

$5P_{3/2}(F' = 4)$ transition in ^{85}Rb, we assemble a Doppler-free spectroscopy apparatus that will provide input to the laser stabilization system. We obtain Doppler-free spectra, first without signal processing and then with lock-in amplification. The first spectra obtained provide further insight into the tuning characteristics of the laser and display potential problems with laser tuning. The signals obtained with lock-in amplification display hyperfine structure of both naturally occurring isotopes of rubidium: ^{87}Rb and ^{85}Rb. The ^{85}Rb spectra can be obtained in minutes using the current experimental setup and are of high enough resolution and amplitude to aid in laser stabilization.

5.2 Experimental Setup

5.2.1 Optical Setup

The basic goal of the experimental setup is to cause pump and probe beams to counterpropagate through a rubidium vapor cell, as shown in Fig. 4.5. Figure 5.1 is a diagram of the experimental setup. The beam output from the Littman TEC 500 diode laser is first reflected by two mirrors (not shown) to adjust the beam height to 4" above the surface of the table. A half-wave plate ($\lambda/2$) is used to attenuate the overall beam power. The Faraday optical isolator (isolator) ensures that the beam does not reflect off of any optics back into the lasing cavity, as this may cause instability in the diode laser output. The isolator also rotates the polarization to vertical. A beam splitter (splitter) divides the power of the beam approximately in half. The transmitted beam is currently blocked, but will be used down the road in laser cooling experiments.

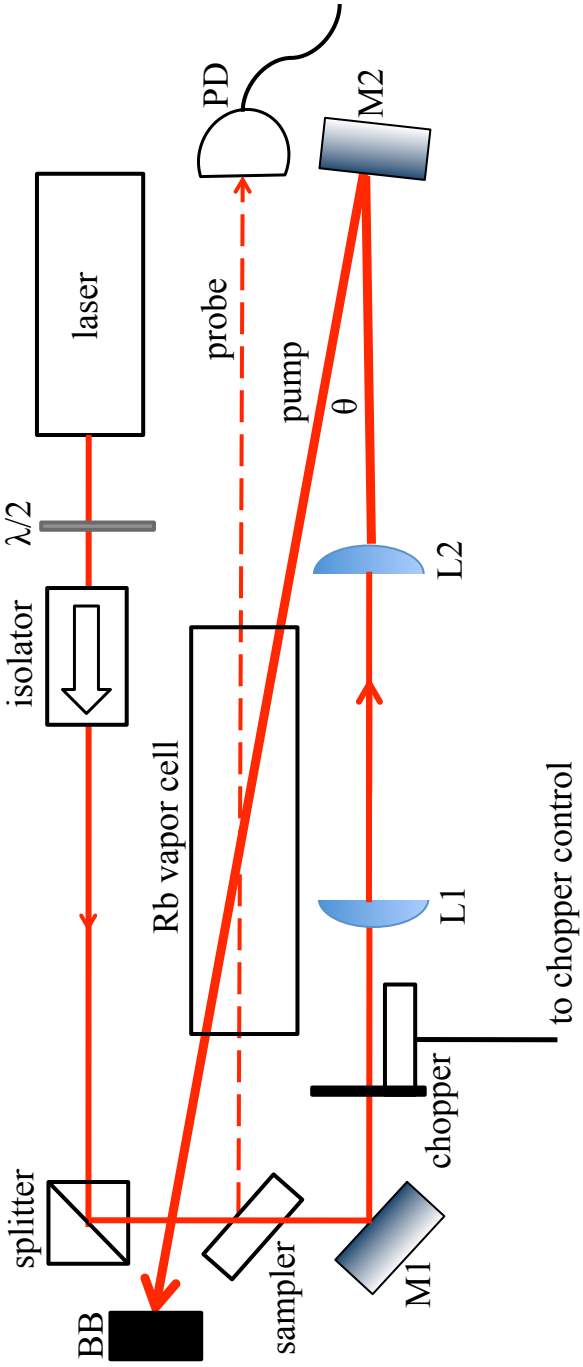

Figure 5.1: Diagram of the Doppler-free spectroscopy experimental setup.

The beam sampler (sampler) plays the crucial role of partitioning the laser beam into a powerful pump beam and a weak probe beam. Approximately 94% of the beam is transmitted and forms the pump, while 6% is reflected as the probe beam toward the rubidium vapor cell. The Opthos Instruments Rb vapor cell used in this experiment is cylindrical, 12" long and 1" in diameter. The probe beam passes through the cell, perpendicular to the end facets, and enters a homemade photodetector (PD) with adjustable gain. The vapor cell contains Rb in its natural abundance, 72.17% ^{85}Rb and 27.83% ^{87}Rb.[24] While ^{85}Rb is the isotope of interest in future laser cooling experiments, we will see that both prove useful in learning about absorption spectroscopy.

The more powerful pump beam is reflected 90° to the chopper, which can be easily removed or remounted. We use the chopper to obtain high-resolution spectra of hyperfine structure but remove it when obtaining more "coarse" spectra. We will discuss this difference in setup more in section 5.3. Several features in this setup serve to increase the amount of overlap of the pump and probe beams as they propagate in opposite directions through the vapor cell, thereby increasing the number of atoms with which the beams interact simultaneously. First, two plano-convex lenses (L1 and L2) are used to increase the radius of the pump beam by a factor of approximately two.[1] Clearly, increasing the area of the pump beam makes it easier to overlap the two beams in the cell. Secondly, the angle θ in Fig. 5.1 was made to be approximately 2.5° to make the beams as close to antiparallel as possible after the pump reflects off of M2.

5.2.2 Electronics Setup

The electronics setup can be divided into two components: laser control and data acquisition (Fig. 5.2). The laser controls were discussed in detail in Chapter 3, but

[1]The probe beam has a radius of 0.8 mm and the pump beam is 1.4 mm in radius.

have been modified slightly for use in the experiment. The voltage across the piezo-actuator can be set by hand to a DC offset level, but a Hewlett Packard Model 310B function generator provides a ramp wave to the piezo-actuator controls for frequency control of the laser output. Increasing the amplitude and period of the triangle wave increases the range of laser output frequency and the rate at which the laser scans through frequency.

The photodiode voltage signal is proportional to the probe power that is transmitted through the Rb vapor cell.[2] When obtaining high-resolution spectra of hyperfine structure, the photodiode signal serves as the input to a SRS Model SR530 lock-in amplifier, as shown in Fig. 5.2. We use the chopper reference signal as the reference input for the lock-in amplifier. We monitor the output of the lock-in amplifier on a TDS 3012C oscilloscope that is triggered by the function generator output. We collect the data for analysis using Tektronix Open Choice Desktop software.

[2]Note that, while Chapter 4 made reference to curves showing *absorption* of laser light as a function of laser frequency, the photodetector measures the power of the probe beam that is *transmitted* through the gas. The features are still the result of absorption of light by atoms, so we continue to refer to them as *absorption features*.

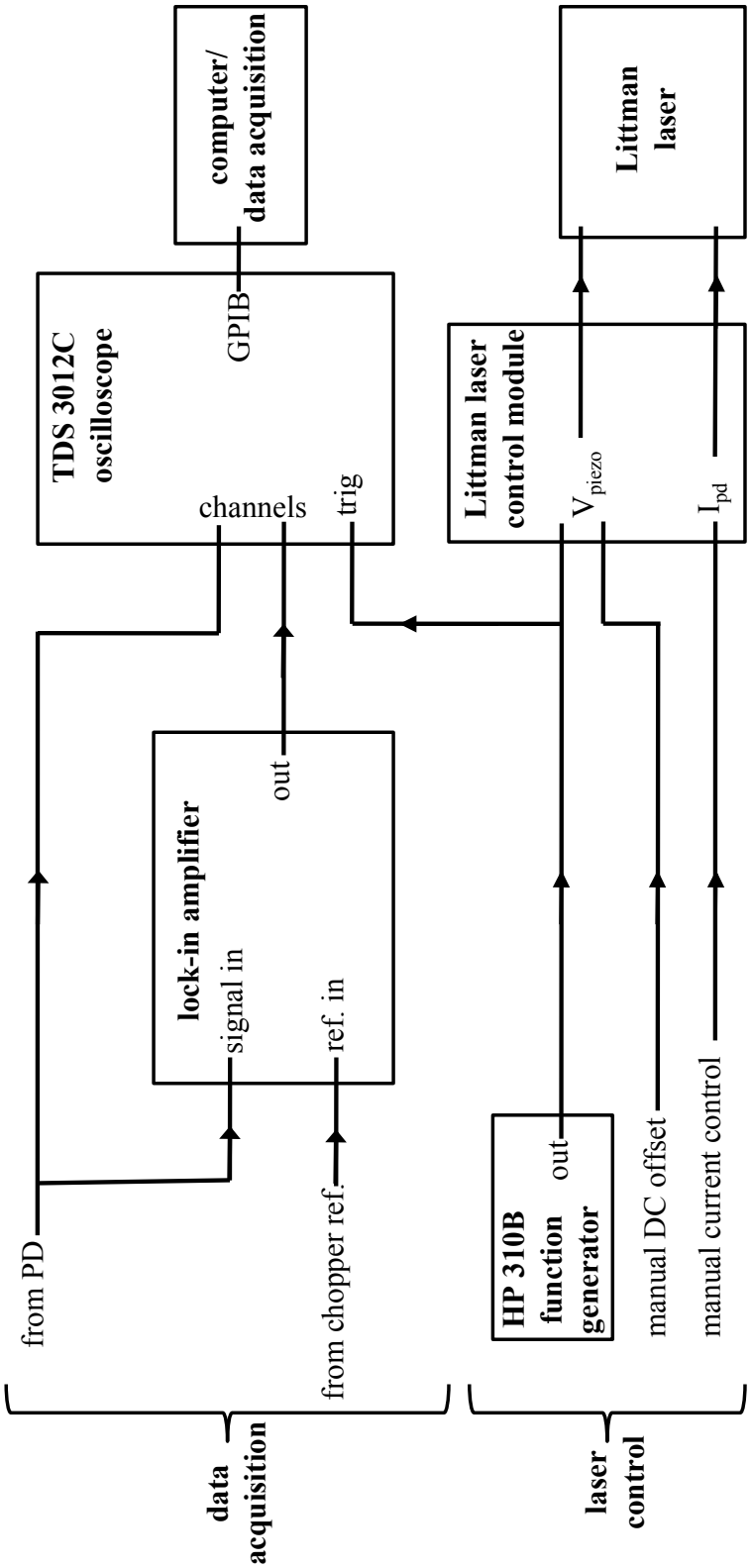

Figure 5.2: Schematic diagram of the electronics setup used for data acquisition and laser control in this experiment.

5.3 Procedure

In studying the function of a diode laser (Chapter 3), we learned that the laser produces multiple modes at certain combinations of injection current, piezo-actuator voltage, and temperature. When scanning over a range of frequencies, we see a related behavior that manifests itself as discontinuous frequency output, known as mode-hopping. When trying to obtain spectra that display absorption of the probe beam as a function of laser frequency, discontinuities in laser frequency are undesirable.

Thus, the first step in obtaining Doppler-free spectra is to find a temperature, injection current, and piezo-actuator voltage range over which the laser can vary in frequency continuously. We first find a piezo-actuator voltage range for which the laser outputs a frequency that matches a resonance transition of the Rb in the cell. To do this, we rotate the waveplate to transmit maximum power, turn the lock-in amplifier off, and remove the chopper. With the setup simplified, we view the cell through an infrared (IR) viewer and manually tune the piezo-actuator voltage until we view strong fluorescence in the cell. We then set the function generator to output a triangle wave roughly 5 V peak-to-peak and several tens of Hz in frequency. While the piezo voltage is modulated, we view the photodiode signal on the oscilloscope, which measures the probe power transmitted as a function of laser frequency. Figure 5.3 shows one such transmission spectrum. For a wide enough scan, the laser mode hops back down to a lower frequency, resulting in multiple iterations of the same spectral features, as Fig. 5.3 illustrates. While viewing the spectrum on the oscilloscope, we manually adjust the piezo-actuator voltage and injection current until the laser scans continuously over the desired frequency range. The spectra must be monitored on the oscilloscope as adjustments are continuously made to the injection current and piezo-actuator voltage.

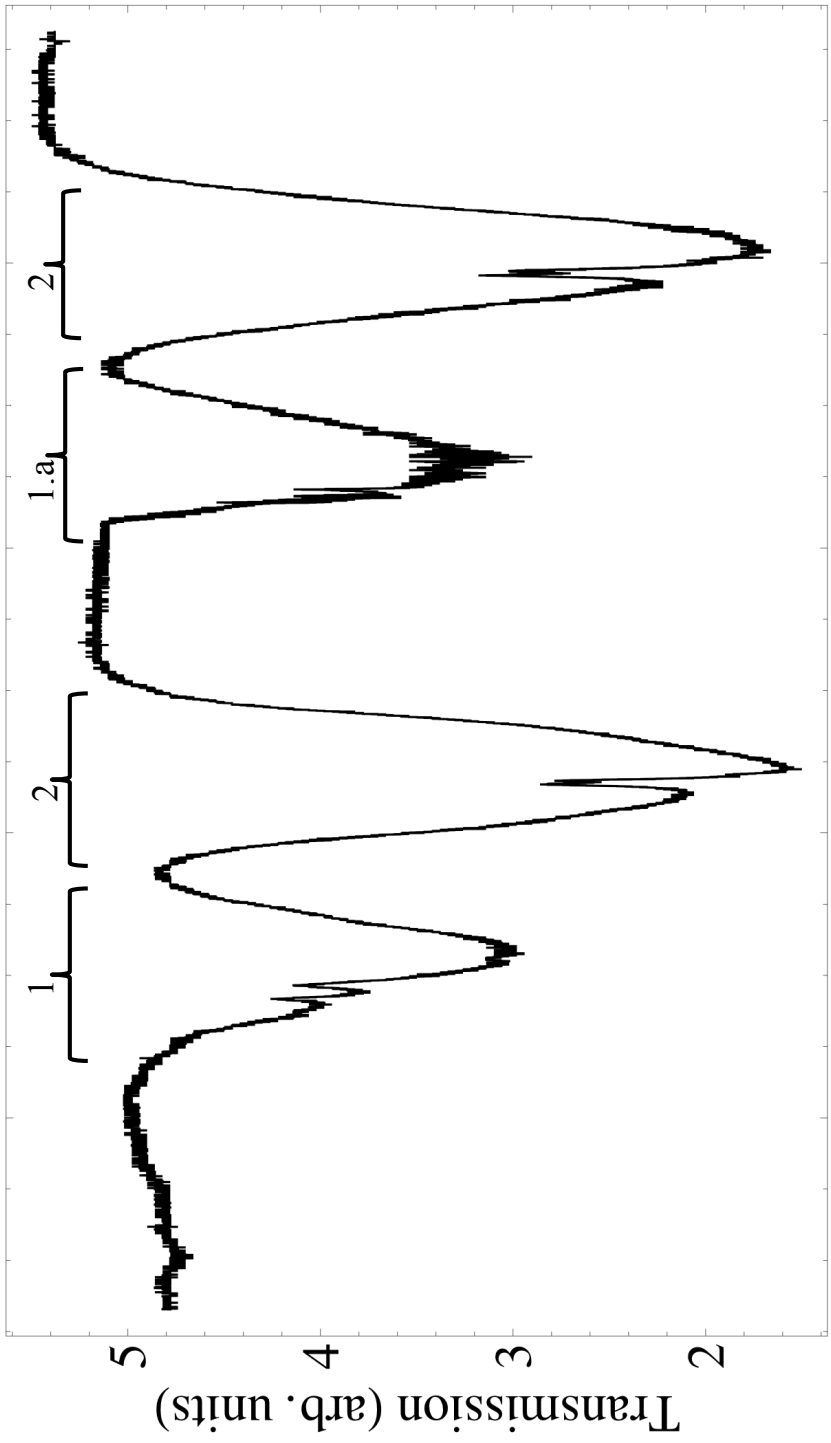

Figure 5.3: Transmission spectra displaying two iterations of ^{87}Rb and ^{85}Rb spectral features, as well as mode-hopping. The labeled features are the (1.) ^{87}Rb $5S_{1/2} \rightarrow 5P_{3/2}$ transition, (1.a.) ^{87}Rb $5S_{1/2} \rightarrow 5P_{3/2}$ transition, with features obscured by a region of mode-hopping, and (2.) ^{85}Rb $5S_{1/2} \rightarrow 5P_{3/2}$ tansitions. The frequency scale is given relative to the ^{85}Rb $5S_{1/2}(F = 3) \rightarrow 5P_{3/2}(F' = 4)$ transition. (Due to mode-hopping, the frequency is discontinuous and should only be used to to guide the eye in gauging relative separations between peaks for which no mode-hopping occurs.)

If settings that result in a continuous frequency scan can't be attained, it may be necessary to change the laser diode temperature, by 0.5°C for example, and repeat the process outlined in the previous paragraph. We found that the TEC 500 undergoes minimal mode-hopping in the frequency range of interest for a diode temperature of 20.0° C and an injection current of 63 mA. Once a continuous scan has been achieved, we need not adjust the temperature. The settings used in the spectra shown in this chapter are summarized in Table I and are typical of other spectra taken in this project but not discussed here.

Upon finding suitable settings, we then decrease the ramp voltage so that the laser scans over only the desired frequency range. It may be the case that one of the feature iterations in Fig. 5.3 makes for a smoother scan than another, so we choose that spectrum. If mode-hops continue to occur, as in Fig. 5.4, we first adjust the piezo-actuator voltage and then the injection curent, once again.

While viewing the desired spectrum, we optimize the angle θ at which the probe beam enters the Rb vapor cell by adjusting the mirror M3 in Fig. 5.1. We adjust the angle of this mirror until we maximize the amplitude of the Doppler-free features. Minor adjustments in beam overlap can increase or decrease the magnitude of the Doppler-free features. We find it helpful to compare the Doppler-free and Doppler-broadened spectra, such as those in Fig. 5.5, and can transition between the two simply by blocking the pump beam with an index card.

Once we obtain satisfactory coarse spectra, we use the lock-in amplifier and chopper to study the hyperfine structure of a single isotope of Rb with higher-resolution. We modify the experimental setup by putting the chopper in place and setting the chopping frequency using the control module. Because the lock-in signal input requires only a small amplitude signal from the photodetector, we attenuate the overall beam power by rotating the half-wave plate. While incrementally attenuating the overall laser power, we increase the lock-in amplifier sensitivity accordingly. We slow

Table I: Experimental parameters for spectra. For all spectra, the injection current i_{pd} was 63 mA and the diode temperature was 20.0° C. For each scan, the ratio of pump beam intensity to saturation intensity I_{pump}/I_s, the ratio of probe beam intensity to saturation intensity I_{probe}/I_s, the injection current i_{pd}, the piezo-actuator DC offset voltage V_{piezo}, the frequency f_{FG} and peak-to-peak voltage V_{FG} of the triangle wave used for laser frequency output modulation, and the lock-in amplifier sensitivity and time constant τ are listed. For spectra taken without lock-in amplification, the function generator frequency was typically between 1 and 10 Hz. For spectra taken with lock-in amplification, the function generator frequency was about 0.01 Hz and the chopping frequency was about 300 Hz.

Figure	I_{pump}/I_s	I_{probe}/I_s	i_{pd} (mA)	V_{piezo} (V)	f_{FG} (Hz)	V_{FG} (V)	sensitivity (mV)	τ (ms)
5.3	94.5	27.6	63	47.9	1.3	5.28	–	–
5.4	94.5	27.6	65	46.6	5.26	2.20	–	–
5.5	94.5	27.6	63	46.6	5.26	2.20	–	–
5.8	4.8	1.4	63	45.3	0.08	0.648	10	30
5.9	4.8	1.4	63	45.3	0.10	0.430	10	30
5.10	10.6	3.5	63	45.3	0.10	0.430	10	30

the function generator frequency so that the rate at which the laser scans over a given hyperfine structure feature is on the order of ten times the lock-in amplifier time constant. We adjust these settings until we obtain spectra that resolve six Doppler-free features over about 200 MHz for ^{85}Rb and 500 MHz for ^{87}Rb.

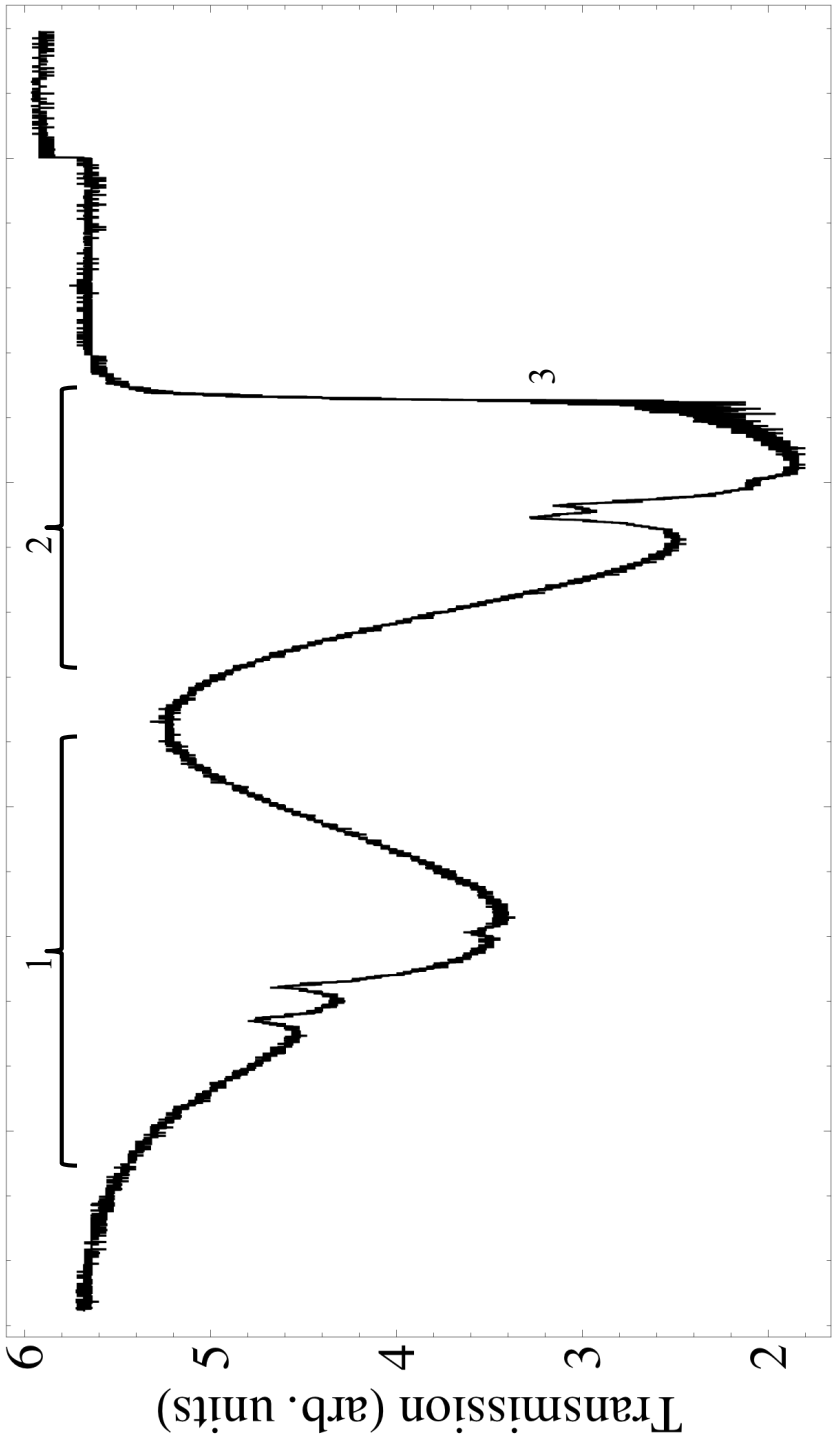

Figure 5.4: Absorption spectra showing ^{87}Rb and ^{85}Rb features, as well as mode-hopping behavior. The labeled features are the (1.) ^{87}Rb $5S_{1/2} \rightarrow 5P_{3/2}$ and (2.) ^{85}Rb $5S_{1/2} \rightarrow 5P_{3/2}$ transitions. A sharp discontinuity occurs during a laser mode-hop at (3.). The frequency scale is given relative to the ^{85}Rb $5S_{1/2}(F = 3) \rightarrow 5P_{3/2}(F' = 4)$ transition. (Again, due to mode-hopping, the frequency scale should be used only as a visual guide.)

5.4 Experimental Results

5.4.1 No Lock-In Amplification

If Chapter 4 was not a convincing argument in favor of Doppler-free spectroscopy techniques, then the juxtaposition of Doppler-free and Doppler-broadened spectra in Fig. 5.5 may speak more eloquently to that point. While hyperfine structure features are still obscured by signal noise in the Doppler-broadened spectrum, we readily resolve several absorption features in the Doppler-free spectrum in Fig. 5.5.[3] As several of these features expose hyperfine structure, Doppler-free spectroscopy puts us closer to our experimental goal.

Still, the dominant absorption features in Fig. 5.5 are crossover peaks, which do not represent the energy of a single hyperfine structure transition. Crossover peaks occur when the pump and probe beams interact with a common group of atoms that are not at rest. Atoms with velocity toward the pump beam observe the pump beam blueshifted to one resonance transition and the probe beam redshifted to a lower-energy resonance. Similarly, atoms with velocity away from the pump beam observe the pump beam redshifted to one resonance transition and the probe beam blueshifted to a higher-energy resonance. This results in crossover peaks centered at a frequency halfway between that of two "real," or direct-transition, peaks. The prominence of the crossover peaks in the spectra shown in Fig. 5.5 obscures the real peaks. Signal noise further obscures the real peaks. Resolving hyperfine structure will require processing the photodetector signal by lock-in amplification.

[3]Taking Doppler-broadened spectra is as simple as blocking the pump beam in a Doppler-free spectroscopy setup.

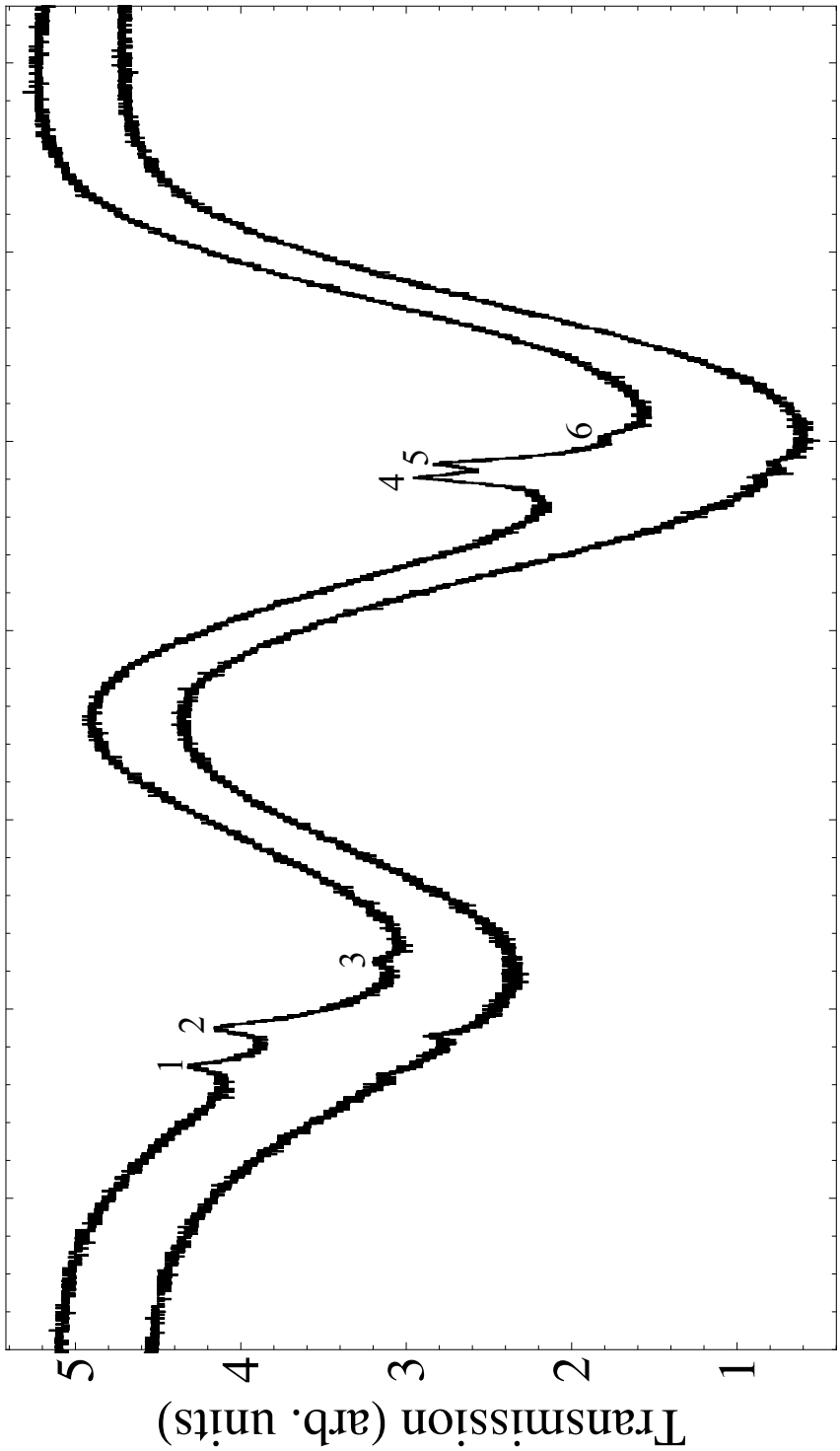

Figure 5.5: Doppler-free saturated-absorption spectrum showing Doppler-broadened (bottom) and Doppler-free spectra (top). The labeled features are the ^{87}Rb $5S_{1/2}(F = 2) \rightarrow 5P_{3/2}$ $[(1.)F' = 1, 3$ crossover, $(2.)F' = 2, 3$ crossover, $(3.)F' = 3]$ and ^{85}Rb $5S_{1/2}(F = 3) \rightarrow 5P_{3/2}$ $[(4.)F' = 2, 4$ crossover, $(5.)F' = 3, 4$ crossover, $(6.)F' = 4]$ transitions. ν_0 represents the ^{85}Rb $5S_{1/2}(F = 3) \rightarrow 5P_{3/2}(F' = 4)$ transition. The Doppler-broadened spectrum has been offset by -0.5 units on the transmission axis.

5.4.2 ^{87}Rb Hyperfine Structure

Figures 5.6 and 5.7 are energy level diagrams for the two naturally occurring isotopes of rubidium. These show that the relative spacing between hyperfine energy levels in ^{87}Rb is greater than the spacings in ^{85}Rb. The natural extension of this observation to our experiment leads us to expect that the peaks in our spectra for ^{87}Rb will be spaced farther apart, and therefore easier to resolve than those in ^{85}Rb. Because of this property of the ^{87}Rb isotope, we choose to study it first in order to gauge the resolution of which our setup is capable and determine optimal experimental parameters.

The improvements in resolution of the hyperfine structure features of ^{87}Rb using beam chopping and lock-in amplification are immediately apparent when observing the spectrum in Fig. 5.8. This spectrum shows three crossover peaks, along with three hyperfine structure features for transitions from the $(5S_{1/2},\ F = 2)$ ground state, identified in Fig. 5.8. While the crossover peaks are still much higher amplitude than the hyperfine structure features, we now resolve hyperfine structure features that were entirely obscured by the combined effect of the dominant crossover peaks and signal noise when lock-in amplification was not used (Fig. 5.5). Although it is not indicative of a single hyperfine structure transition, the prominent $F' = 2, 3$ crossover peak is a good gauge for the resolution of our spectra, with a linewidth of 40 ± 4 MHz.

The ^{87}Rb absorption features are a convenient checkpoint in this experiment because they are only about 1 GHz (Fig. 5.5) lower in frequency than the ^{85}Rb features. Switching between spectra of the two isotopes requires no change to the experimental setup and we can make the necessary electronics adjustments in minutes. This spectrum exposes the current capabilities of our experimental method and enables us to better study the isotope of Rb that will be used in laser cooling.

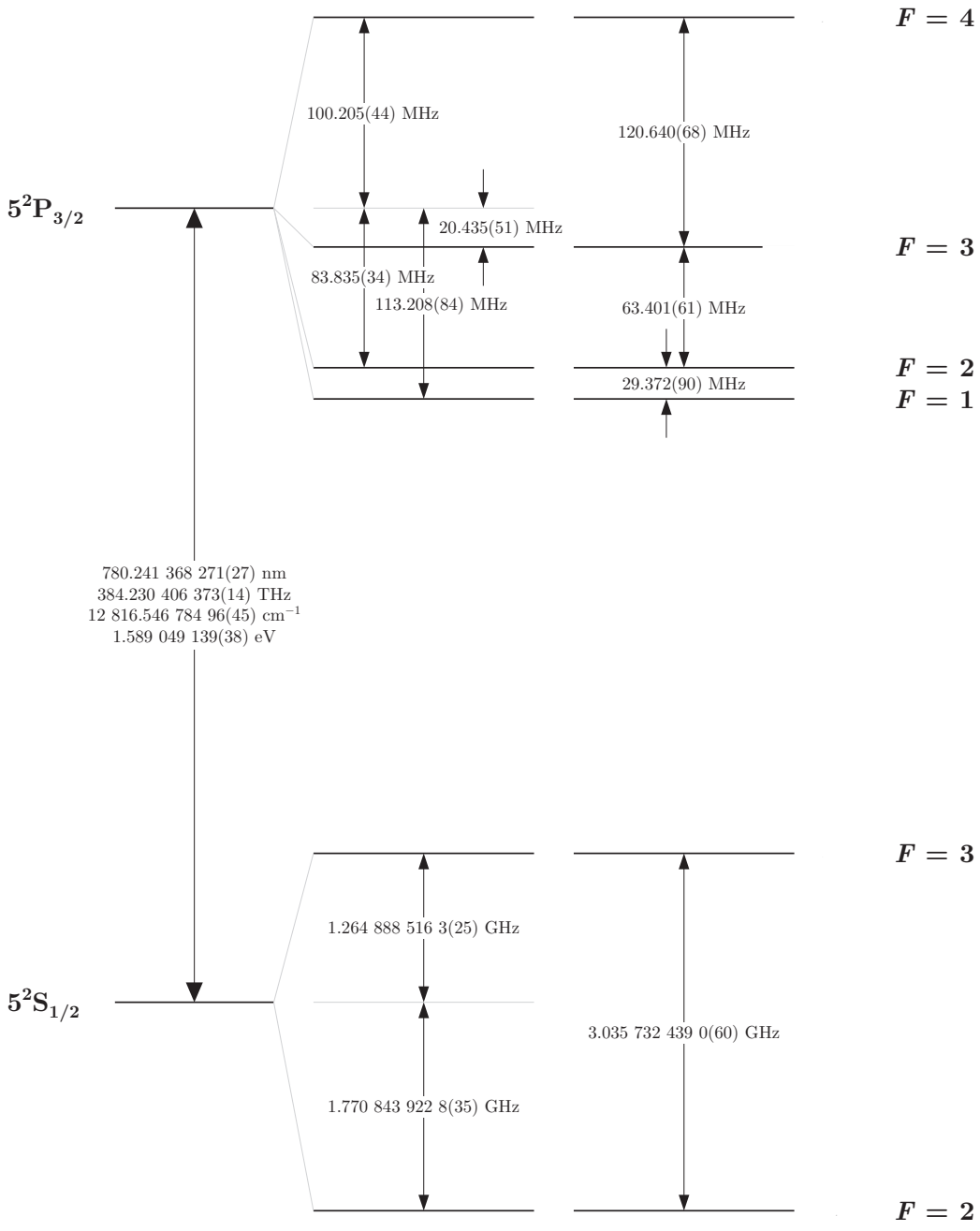

Figure 5.6: Energy level diagram for ^{85}Rb (after ref. [18]), as in Fig. 4.1.

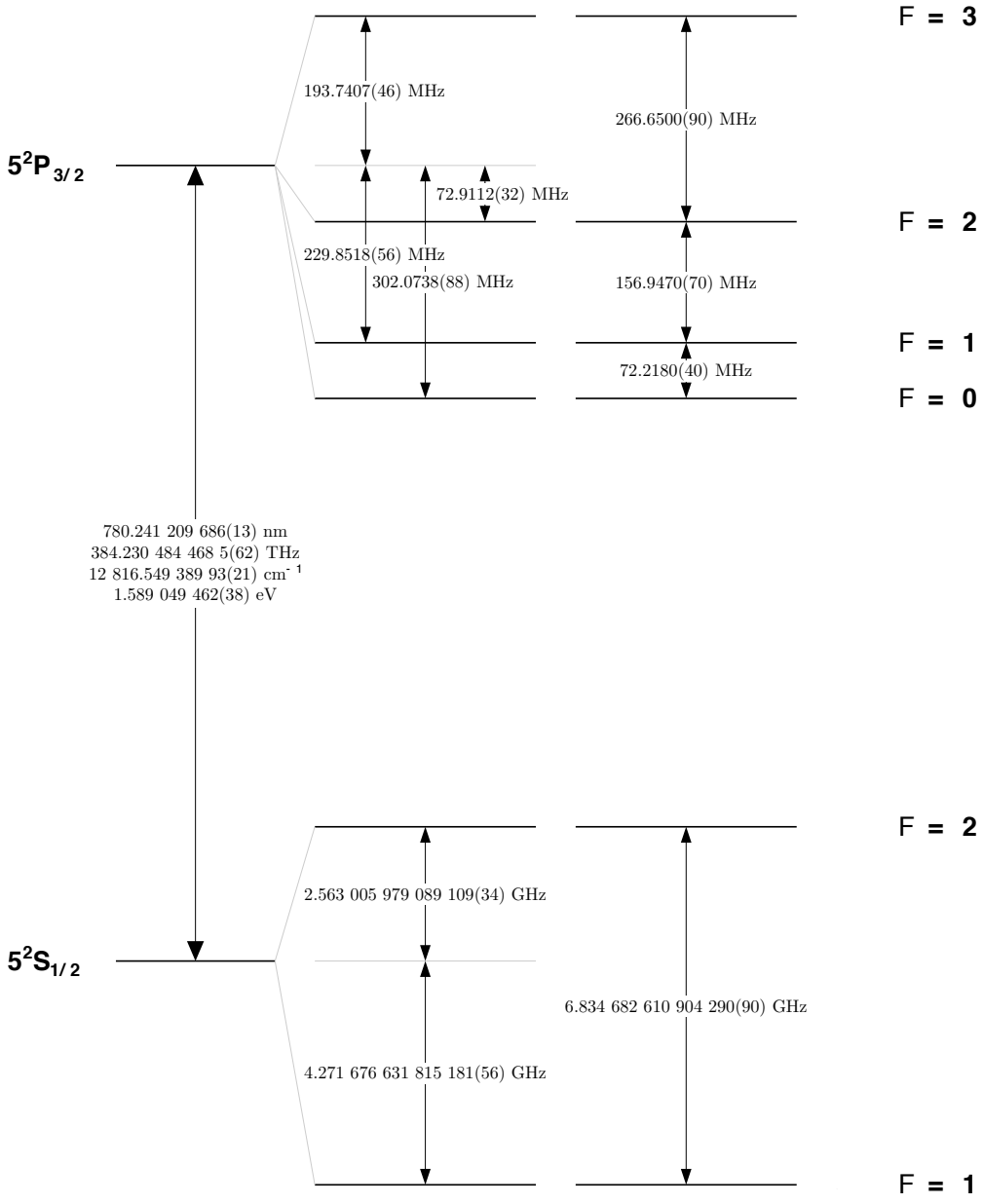

Figure 5.7: Energy level diagram for ^{87}Rb (after ref. [19]).

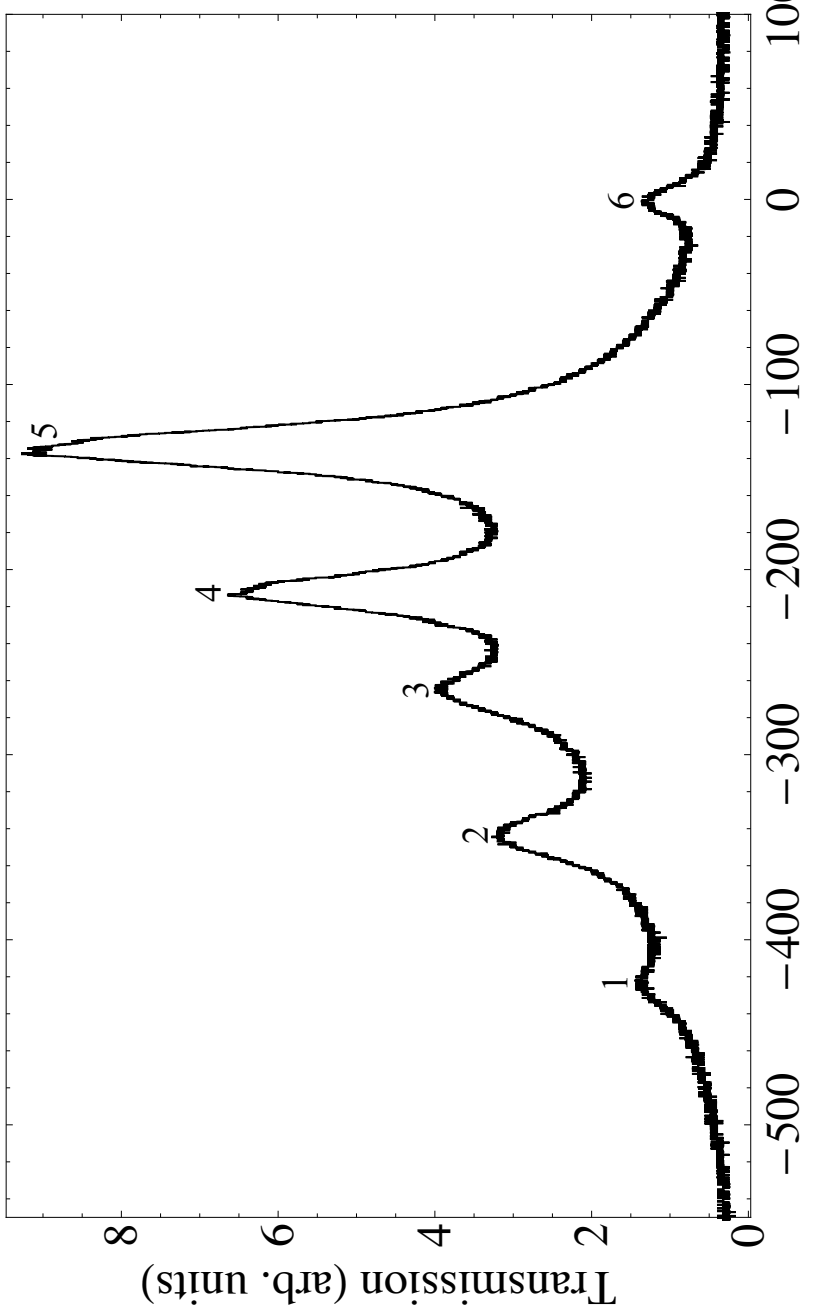

Figure 5.8: Doppler-free saturated-absorption spectrum of ^{87}Rb hyperfine structure. The labeled features are the ^{87}Rb $5S_{1/2}(F = 2) \rightarrow 5P_{3/2}$ [(1.)$F' = 1$, (2.)$F' = 1, 2$ crossover, (3.)$F' = 2$, (4.)$F' = 1, 3$ crossover, (5.)$F' = 2, 3$ crossover, (6.)$F' = 3$)] transitions. The frequency scale is given relative to the ^{87}Rb $5S_{1/2}(F = 2) \rightarrow 5P_{3/2}(F' = 3)$ transition.

5.4.3 ^{85}Rb Hyperfine Structure

Figure 5.9 is our Doppler-free spectrum showing ^{85}Rb hyperfine structure for transitions from the $(5S_{1/2},\ F = 3)$ ground state. Again, we resolve three hyperfine transitions and three crossover peaks. When compared with Fig. 5.5, the lock-in amplified spectrum in Fig. 5.9 reveals two more hyperfine structure features and one more crossover peak for this ground state. As we expected, the relative proximity in frequency of the ^{85}Rb peaks (Fig. 5.9) reduces our ability to resolve between peaks, when compared with the ^{87}Rb peaks. Still, our goal is to acquire spectra that can be used in a future laser stabilization project and the steep sides of the crossover peaks show promise for use to this end, as we will discuss in section 5.5.

We also investigated the effects of laser power on the resolution of the transmission spectra. For the spectrum in Fig. 5.9, the pump beam was about 8 times the saturation intensity (I_s) for the transition and the probe beam was about $1.4I_s$. This experimental parameter adheres closely to those used in similar experiments, which recommend using a probe beam intensity of about $2I_s$.[4] [25] Figure 5.10 shows the effect of proportionally increasing both the pump and probe beam powers by rotating the half-wave plate (Fig. 5.1). The pump and probe powers used to obtain this spectra are about $17.6I_s$ and $3.5I_s$, respectively. We observe the effects of power broadening, in which a high intensity laser beam stimulates emission of radiation in atoms of the gas. The effect is to decrease the excitation lifetime of atoms in the gas. As we saw in Chapter 4, the excitation lifetime is inversely related to the linewidth, so power broadening increases the linewidth of spectral features. It also seems to increase the amplitude of the crossover peaks relative to the direct transition peaks.

[4]The saturation intensity for the ^{85}Rb $5S_{1/2}(F = 3,\ \mathrm{m}_F = \pm 3) \rightarrow 5P_{3/2}(F' = 4,\ \mathrm{m}'_F = \pm 3)$ transition in ^{85}Rb is 1.66932(35) mW/cm^2.[18]

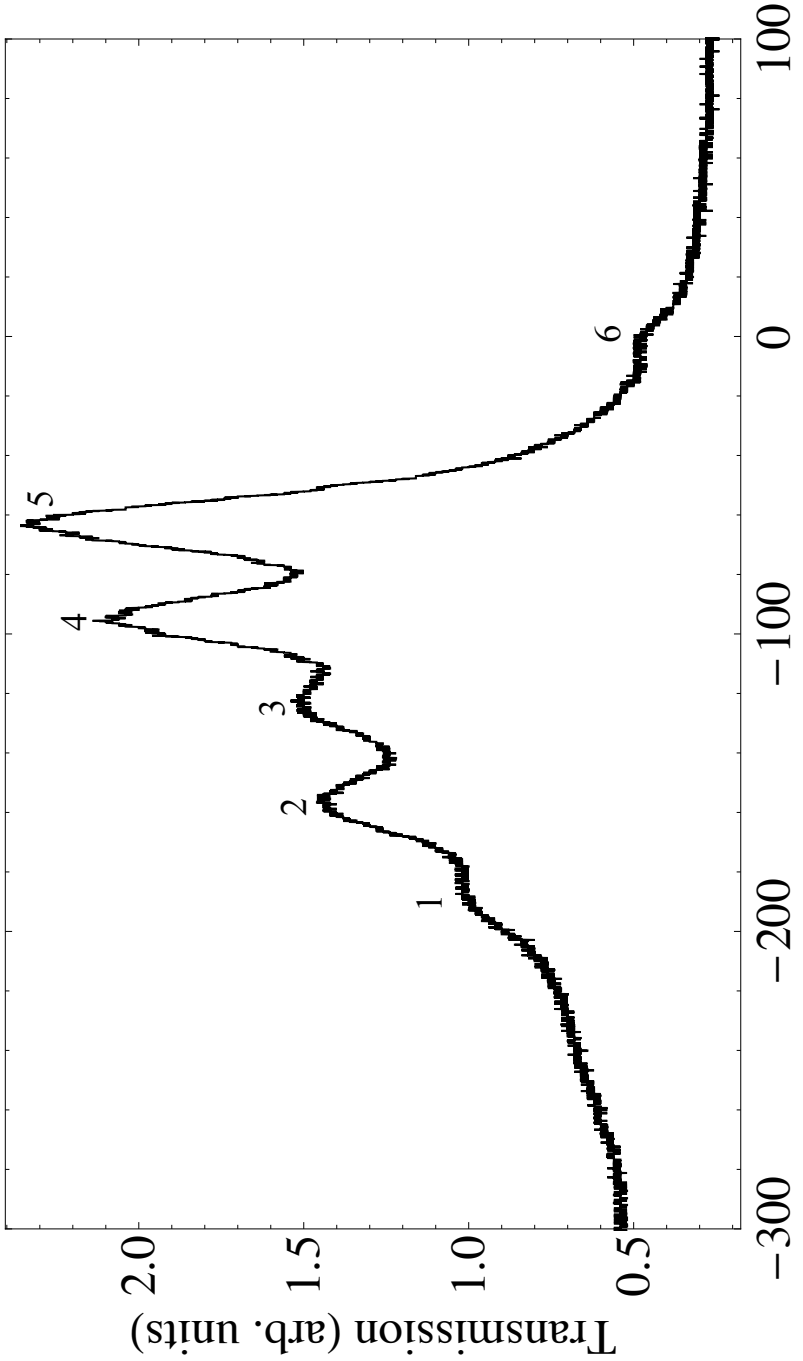

Figure 5.9: Doppler-free saturated-absorption spectrum of ^{85}Rb hyperfine structure. The labeled features are the ^{85}Rb $5S_{1/2}(F = 3) \rightarrow 5P_{3/2}$ [$(1.)F' = 2$, $(2.)F' = 2, 3$ crossover, $(3.)F' = 3$, $(4.)F' = 2, 4$ crossover, $(5.)F' = 3, 4$ crossover, $(6.)F' = 4$)] transitions. The frequency scale is given relative to the ^{85}Rb $5S_{1/2}(F = 2) \rightarrow 5P_{3/2}(F' = 4)$ transition.

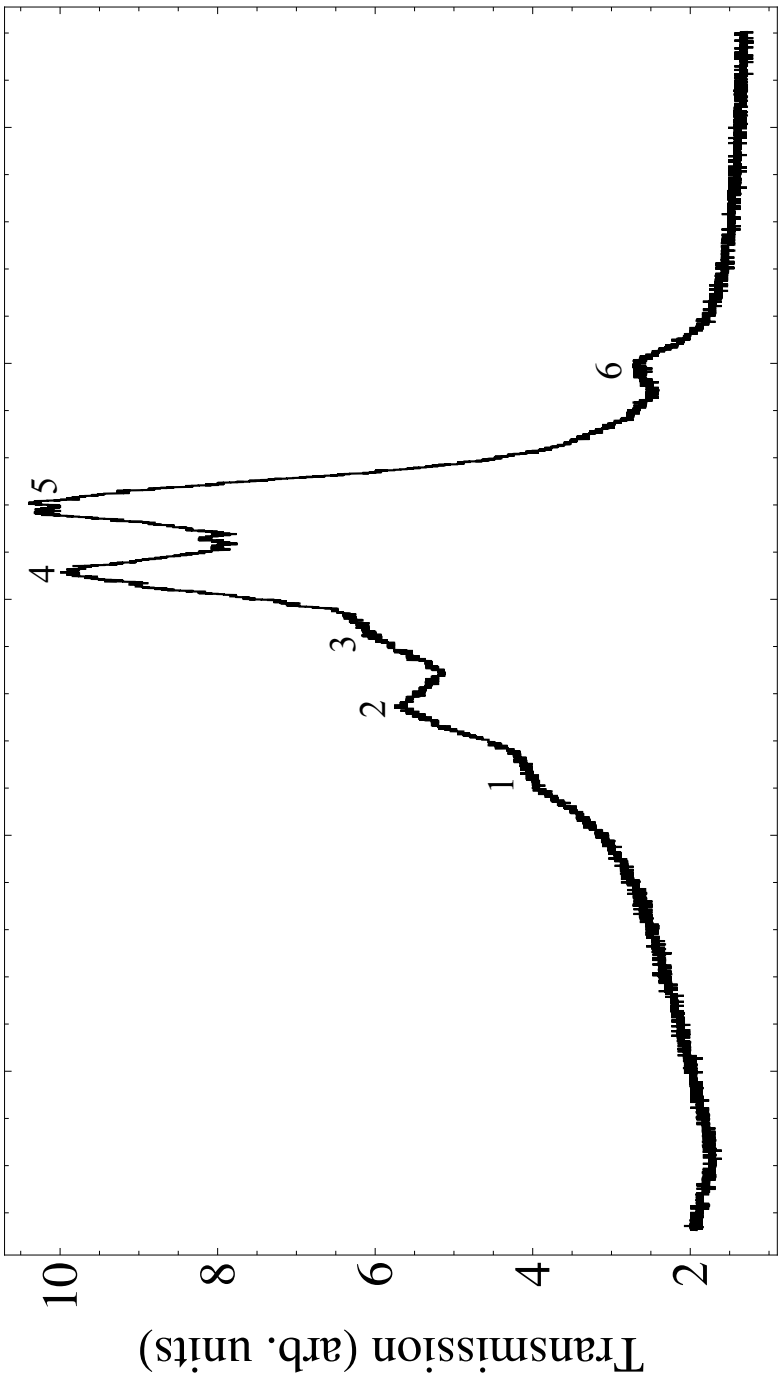

Figure 5.10: Doppler-free saturated-absorption spectrum exhibiting power broadening in ^{85}Rb hyperfine structure. The labeled features are the ^{85}Rb $5S_{1/2}(F = 3) \rightarrow 5P_{3/2}$ $[(1.)F' = 2$,$(2.)F' = 2, 3$ crossover, $(3.)F' = 3$, $(4.)F' = 2, 4$ crossover, $(5.)F' = 3, 4$ crossover, $(6.)F' = 4)]$ transitions. The frequency scale is given relative to the ^{87}Rb $5S_{1/2}(F = 2) \rightarrow 5P_{3/2}(F' = 3)$ transition.

5.5 Discussion and Future Work

The spectra obtained here display how the Doppler-free spectroscopy experiments we used vastly improve the resolution of transmission spectra. We demonstrate the ability to resolve hyperfine structure features in both naturally occurring isotopes of rubidium. While the crossover peaks are certainly the most prominent features in our spectra, we can use this to our advantage. Electronic stabilization units are typically able to lock onto features with large negative or positive derivatives. For this reason, we believe that spectra like the ones obtained here will serve as an adequate feedback signal for laser-stabilization electronics.

Still, several improvements to the existing Doppler-free spectroscopy setup may merit investigation. First of all, the optics table should be floated to minimize the effects of mechanical vibrations in the laboratory and the building. Another potential avenue for improvement is to study the effects of varying the relative pump and probe intensities. Previous works suggest that an optimal ratio of pump to probe intensity may improve resolution of hyperfine spectral features. [26] The heavy lifting in this spectroscopy experiment is done; we aligned the optics, set up the electronics, and after much ado, found laser settings that output radiation continuously over the frequency range of interest. With the existing setup, spectroscopy experiments can be easily repeated, and systematically varying these experimental parameters should not be an immense undertaking.

A laser stabilization module is in the mail. We chose the Sacher LB2001 High-Speed Dual Path Servo Controller for its compatibility with our Sacher diode laser and potential ease of use with our spectroscopy experimental setup. Its features include the ability to lock the laser output to the side of a peak. This is promising for laser stabilization because of the prominence of the $F' = 3, 4$ crossover peak adjacent to the ^{85}Rb $5S_{1/2}(F = 3) \rightarrow 5P_{3/2}(F' = 4)$ transition in Figs. 5.9 and 5.10. The output frequency of the laser may then be shifted to the correct $F' = 4$ transition frequency

using an acousto-optical modulator. The extent of our experimental work for this project ends with Doppler-free spectroscopy and we allocate laser stabilization, the next step down the road to laser cooling, to future work.

Chapter 6

Laser Cooling

Once the laser has been stabilized, the next step is to begin assembly of the laser cooling apparatus. Indeed, there is still extensive work to be done before this can happen and it is far beyond the scope of this project, experimentally. Nevertheless, this chapter may be considered optional reading, perhaps as a primer for the physics underlying laser cooling, to satisfy curiosity, or to put the eventual goals of the project on one's radar.

In this chapter, I describe the theory of how radiation exerts forces on atoms in a dilute gas such as rubidium vapor. The use of radiation pressure alone to cool a gas creates a slowly-moving ensemble of atoms that is known as "optical molasses." Although optical molasses is a laser-cooled gas, it is not confined spatially. One technique of trapping atoms, explored here, is the use of a magneto-optical trap (MOT), which exploits the hyperfine structure of the atom in order to generate a spatially-dependent force on cold atoms.

6.1 Optical Molasses

In Chapter 4, I discussed how an atom with non-zero velocity $\vec{v}$ in a gas will see the laser frequency ω_L Doppler shifted. For laser light of wave-vector $\vec{k}$ incident upon

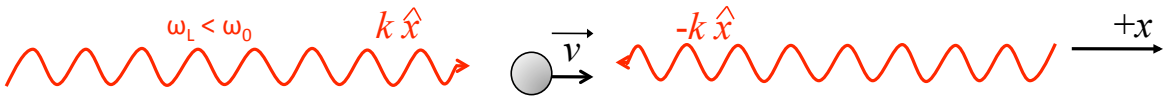

Figure 6.1: An atom with counter-propagating laser beams incident upon it.

such an atom, the observed shift in frequency is $\vec{k} \cdot \vec{v}$. Let us consider the case in which the laser is tuned below the resonant frequency, or red-detuned, and is incident upon a one-dimensional gas, as shown in Fig. 6.1. If two beams counter-propagate as they do in a laser-cooling apparatus, then the atom is more likely to absorb a photon from the beam with wave-vector opposite to its velocity because it will see the radiation blue-shifted toward resonance.

During each scattering event, that is the absorption and emission of a photon, linear momentum is conserved. Therefore, the atom's change in momentum is equal to the momentum carried by the absorbed or emitted photon:

$$\begin{aligned} \Delta\vec{p} &= \Delta\vec{p}_{absorbed} + \Delta\vec{p}_{emitted} \\ &= \hbar\vec{k}_{absorbed} + \hbar\vec{k}_{emitted}. \end{aligned}$$

The atom absorbs a photon from the laser beam and experiences a change in momentum in the direction of laser beam propagation. Because an atom emits photons isotropically, the change in momentum due to emission averages to zero and the total change in momentum, on average, is in the direction of propagation of the absorbed photon:

$$\langle \Delta\vec{p} \rangle = \hbar\vec{k}_{absorbed}.$$

According to Newton's second law, if the momentum of an atom changes with time, there is a net force acting upon the atom: $\vec{F} = \frac{d\vec{p}}{dt}$. As we've seen already, an atom's change in momentum during absorption is equal to the momentum carried by the absorbed photon. Only an atom in the excited state has absorbed a photon and

experienced a force due to the incident laser beam. Therefore, the average amount of momentum delivered to the atom through absorption is equal to the amount of momentum delivered by a photon times the probability ρ_{ee} that the atom absorbed the photon, i.e. the probability of finding that atom in the excited state.

The probability ρ_{ee} that the atom has absorbed the photon must depend upon the rate at which absorption events occur. This rate is given by the inverse of the decay rate $(2\delta\omega_0)^{-1}$.[1] In Chapter 4, we saw that the absorption is a function of frequency. It seems sensible, then, that ρ_{ee} depends upon the laser detuning $\Delta_0 = \omega_L - \omega_0$. Conversely, for fixed laser detuning, the probability that an atom becomes excited depends upon its velocity, as an atom sees a Doppler shift in the incident radiation of $\vec{k}\cdot\vec{v}$. Furthermore, the intensity of the radiation should affect whether or not an atom becomes excited; higher intensity means that more photons will be incident upon the atom, thereby increasing the probability of excitation, until absorption is saturated. These factors affecting the probability of excited state occupancy are combined in the expression for ρ_{ee},[2] [20] [21]

$$\rho_{ee} = \frac{s_0/2}{1 + s_0 + \left(\frac{\Delta}{\delta\omega_0}\right)^2}. \tag{6.1}$$

In the expression above, s_0 is the ratio of the laser intensity I_L to the saturation intensity I_s:

$$s_0 \equiv \frac{I_L}{I_s} = \frac{|\Omega|^2}{2\left(\delta\omega_0\right)^2}. \tag{6.2}$$

The quantity Ω in Eq. 6.2 is the Rabi Frequency, a measure of the coupling between the electric field of an electromagnetic wave and the atom.[3] [21] I will refer to Δ as

[1] For the $\left(5S_{1/2} \rightarrow 5P_{3/2}\right)$ transition in ^{85}Rb, the decay rate is $2\delta\omega_0 = 2\pi \cdot 6.0666(18)$ MHz. [18]

[2] ρ_{ee} is a diagonal element of the density matrix. For a complete derivation of the density matrix, see [20]. For values of the density matrix elements associate with ^{85}Rb, see [18].

[3] Rabi solved the differential equations that described the coupling between the Hamiltonian for the electric field of an electomagnetic wave and the quantum mechanical wavefunction for an electron bound to an atom. For a more thorough description of the Rabi Frequency see [20].

the "effective detuning" experienced by an atom:

$$\Delta = \Delta_0 - \vec{k} \cdot \vec{v}. \tag{6.3}$$

Note that Δ is smallest when the Doppler shift matches the laser detuning and that, for an atom with zero velocity, the effective detuning Δ reduces to the laser detuning Δ_0.

Scattering events occur at a rate $\rho_{ee}(2\delta\omega_0)$, each of which has a change in momentum of $\hbar\vec{k}$. Therefore, [21] [27]

$$\begin{aligned} \vec{F} &= \frac{\Delta\vec{p}}{\Delta t} && (6.4)\\ &= \left(\hbar\vec{k}\right)\left(\rho_{ee}\left(2\delta\omega_0\right)\right) && (6.5)\\ &= \hbar\vec{k}\frac{\delta\omega_0 s_0}{1 + s_0 + \left(\frac{\Delta}{\delta\omega_0}\right)^2}. && (6.6) \end{aligned}$$

Some features of this force are worth noting. Foremost, the direction of the force is the same as that of the incident photon. Secondly, the force does not depend on the atom's position in space. Figure 6.2 shows the effect of increasing s_0, the ratio of incident laser beam intensity to the saturation intensity of the gas. The force is at half of its maximum value when $s_0 = 1$ and has reached 90% of its maximum value when $s_0 = 9$. In the long run, the force increases only modestly with large increases in laser beam intensity. Figure 6.3 shows the force as a function of the ratio of detuning Δ to the half-width at half-maximum $\delta\omega_0$ of the transition for an atom at rest with $s_0 = 1$. We see here that the force on an atom has the same dependence on detuning as does absorption; both have the form of a Lorentzian function.

When the temperature of a gas of atoms becomes low enough, Eq. 6.6 reduces to a more recognizable form. For a fixed detuning, when atoms in a gas slow down, the Doppler shift in frequency becomes much smaller than the detuning of the laser:

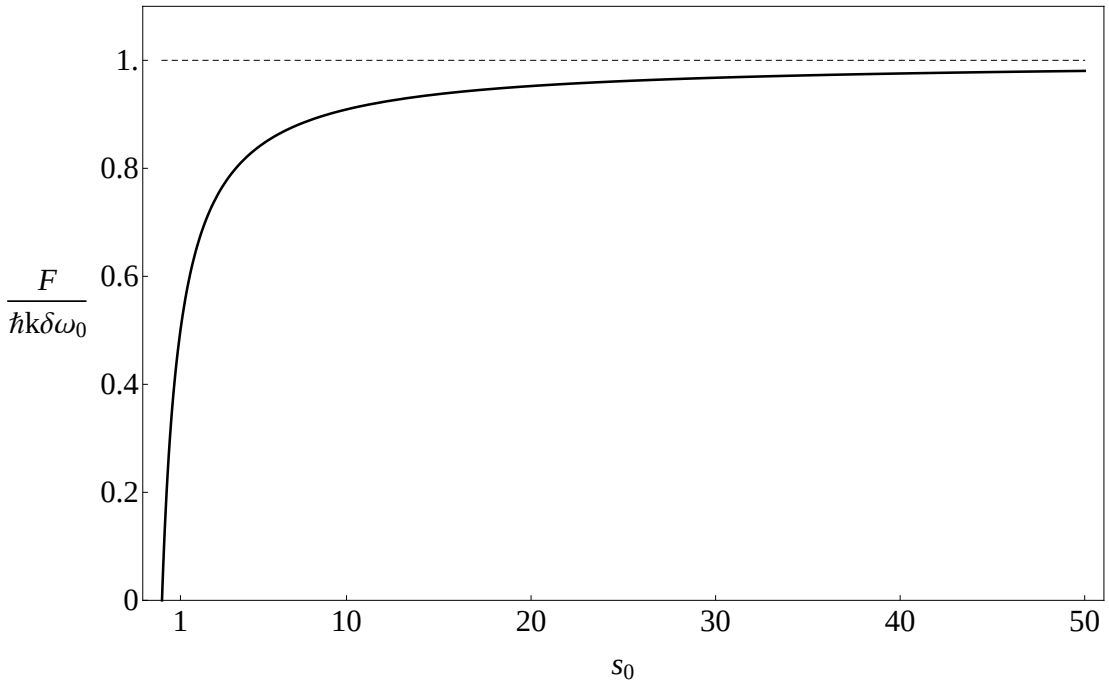

Figure 6.2: The magnitude of the force (Eq. 6.6) on an atom at rest, with $\Delta_0 = 0$, as a function of intensity.

$\left|\vec{k}\cdot\vec{v}\right| \ll \Delta$. The Doppler shift in this limit also becomes much less than the natural linewidth of the atomic transition: $\left|\vec{k}\cdot\vec{v}\right| \ll 2\delta\omega_0$. In this limit,[27]

$$F = 4\hbar k s_0 \frac{\Delta/\delta\omega_0}{\left[1+\left(\frac{\Delta}{\delta\omega_0}\right)^2\right]^2} kv \tag{6.7}$$

$$= -\beta v, \tag{6.8}$$

where

$$\beta \equiv 4\hbar k^2 s_0 \frac{\Delta/\delta\omega_0}{\left[1+\left(\frac{\Delta}{\delta\omega_0}\right)^2\right]^2}.$$

For atoms with low velocity, we see that the force on an atom can be approximated by a dissipative force that is proportional to velocity.

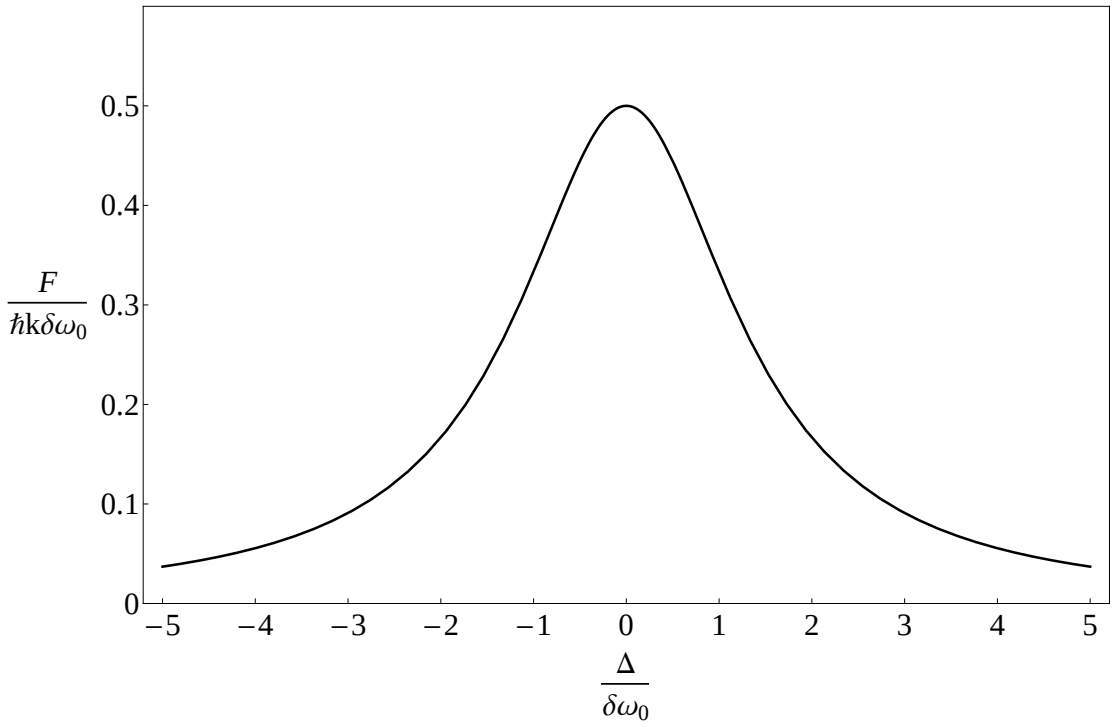

Figure 6.3: Magnitude of the force (Eq. 6.6) on an atom due to an electromagnetic wave as a function of the ratio of detuning Δ to half of the natural linewidth $\delta\omega_0$, represented by the dimensionless parameters $\frac{F}{\hbar k \delta\omega_0}$ and s_0. Here, s_0 is taken to be one.

6.2 The Doppler Limit

When deriving an expression for the force, I considered the time-averaged momentum due to scattering events. Although the force described in the previous section dissipates kinetic energy from the atoms, I have not yet accounted for the random nature of the scattering processes; quantum fluctuations in these events cause heating in the gas. In this section, we see that there is a quantum limit in temperature when cooling a gas by radiation pressure alone.

Consider a particle in a one-dimensional gas, as in Fig. 6.1, but with zero velocity. The change in momentum of this particle can be modeled by a random walk; the atom is equally likely to absorb from the beam traveling to the right as it is to absorb from the beam traveling to the left. Indeed, the expectation value for the net change

in momentum of the atom in this case is zero: $\langle p \rangle = 0$. The expected value of the square of momentum, however, is not zero: $\langle p^2 \rangle = (\hbar k)^2$. Calling the total photon scattering rate R due to the two counter-propagating beams, [27]

$$\frac{d\langle p^2 \rangle}{dt} = 2(\hbar k)^2 R. \tag{6.9}$$

The total scattering rate

$$R \equiv \frac{|F_{left}| + |F_{right}|}{\hbar k} \tag{6.10}$$

is simply the sum of the magnitudes of the force on the atom due to the beam traveling to the left, F_{left}, and that due to the beam traveling to the right, F_{right} divided by the momentum transferred during each scattering event. For the one-dimensional random walk, there are an average of two steps per scattering event, which introduces the factor of two in Eq. 6.9.

Because kinetic energy is proportional to p^2, the randomness of the scattering events leads to an increase in the kinetic energy of the atoms in a gas, or heating:

$$\left(\frac{dK}{dt}\right)_{heating} = \frac{d}{dt}\frac{\langle p^2 \rangle}{2m_a} \tag{6.11}$$

$$= \frac{(\hbar k)^2}{m_a} R \tag{6.12}$$

$$= \frac{(\hbar k)^2}{m_a} \frac{2\delta\omega_0 s_0}{1 + \left(\frac{\Delta}{\delta\omega_0}\right)^2}. \tag{6.13}$$

In the third equality, I substituted for the total scattering rate R (Eq. 6.10), but used the low-temperature approximation discussed in the previous section. When the system is at thermodynamic equilibrium, the contribution to the kinetic energy due to heating equals that due to the dissipative cooling force: [27]

$$\frac{(\hbar k)^2}{m_a} \frac{2\delta\omega_0 s_0}{1 + \left(\frac{\Delta}{\delta\omega_0}\right)^2} = -\beta\langle v^2 \rangle, \tag{6.14}$$

so that

$$\langle v^2 \rangle = \frac{\hbar \delta\omega_0}{2m_a} \frac{1 + \Delta/\delta\omega_0}{\Delta/\delta\omega_0}. \tag{6.15}$$

Now, the equipartition theorem states that each degree of freedom has $\frac{1}{2}k_B T$ of energy. Equating this with the kinetic energy of an atom in the one-dimensional case,

$$\frac{1}{2}k_B T = \frac{1}{2}m_a \langle v^2 \rangle. \tag{6.16}$$

The mean squared velocity is at a minimum when $\left(\frac{\Delta}{\delta\omega_0}\right) = -1$ so that the temperature of a gas cooled by radiation pressure alone takes on a minimum value T_D of

$$T_D = \frac{\hbar \delta\omega_0}{k_B}. \tag{6.17}$$

For ^{85}Rb, the Doppler limit temperature is $T_D = 145.57\mu K$.[18] We have seen in this section atoms cooled by radiation pressure alone experience a force that is independent of position and that their kinetic energies are subject to the quantum fluctuations inherent in the absorption process. In order to cool this optical molasses further, the atoms must be trapped by a spatially-dependent force.

6.3 The Magneto-Optical Trap

If the random nature of absorption and emission events leads to heating in a gas of atoms, then one might ask if it is possible to make the process less random; that is, to make an atom absorb only a beam that will provide it with a force toward the center of the trap. In 1987, E. L. Raab and a team at AT&T Bell Labs developed an experimental setup called a magneto-optical trap which Zeeman-shifted the energy levels of the atoms in order to create a spatially-dependent trapping force for a gas of cold neutral sodium atoms. In this section, we explore the physics that makes such a trapping configuration possible.

Raab et al. applied a spatially-dependent, external magnetic field to their cold gas of atoms, resulting in Zeeman-shifting and the appearance of hyperfine atomic structure. In section 4.1, we saw that the hyperfine structure energy levels split into $2F + 1$ non-degenerate energy levels in the presence of a magnetic field external to the atom. Each of these splittings has a quantum number m_F associated with it, for the projection of the total atomic angular momentum vector $\vec{F}$ onto an axis parallel to the magnetic field. The shift in energy is given by Eq. 4.8

$$\Delta E = \vec{\mu} \cdot \vec{B}_{ext} = \mu_B B_{ext} g_F m_F, \tag{6.18}$$

where, μ is the total atomic magnetic moment, μ_B is the Bohr Magneton, g_F is the Landé g_F-factor, and B_{ext} is the magnitude of the applied magnetic field. In this section, consider a hypothetical atom with $F = 0$ ground state and $F' = 1$ excited state. In the presence of an external magnetic field, the ground state experiences no Zeeman-shift, while the excited state splits into levels denoted by total magnetic moment quantum numbers $m'_F = \pm 1, 0$. Equation 6.18 shows how the magnitude of this Zeeman-shift in energy depends upon the orientation of the total atomic magnetic moment vector $\vec{\mu}$ in the magnetic field.

The magnetic field configuration that Raab et al. used has become a standard in magneto-optical trapping. For the purposes of this discussion, we will consider an atom at rest in a one-dimensional gas in the presence of a spatially-dependent magnetic field, as shown in Fig. 6.4. The magnetic field points outward from the origin and increases in strength with increasing x so that it is of the form

$$\vec{B}_{ext} = B_0 x \hat{x}, \tag{6.19}$$

where B_0 is a positive constant with dimensions of magnetic field over length. Now, the Zeeman-shift in energy of an atom in the magnetic field $\vec{B}_{ext}$ depends not only

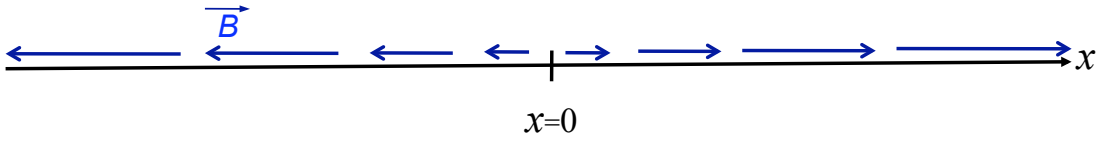

Figure 6.4: The spatial dependence of the magnetic field in a MOT, in the simple case of a one-dimensional gas. The magnitude of the magnetic field B is indicated by the length of the arrows.

upon the orientation of the total atomic magnetic moment in the magnetic field, but also upon the atom's position. Figure 6.5 shows the spatial dependence of the Zeeman-shift in energy for three possible orientations of the total atomic magnetic moment in the magnetic field. For example, an atom in the excited state with $\vec{\mu}$ pointing in the $+\hat{x}$ direction in Fig. 6.4 would experience a positive Zeeman-shift for $x < 0$, zero Zeeman-shift at the origin where $\left|\vec{B}_{ext}\right| = 0$, and a negative Zeeman-shift for $x > 0$.

In the last section, I implicitly discussed the force on an atom when $\vec{B} \neq \vec{0}$. When $\vec{B} \neq \vec{0}$, the effective detuning Δ (Eq. 6.3) is actually [21] [27]

$$\Delta = \Delta_0 - \frac{\vec{\mu} \cdot \vec{B}_{ext}}{\hbar} - \vec{k} \cdot \vec{v}. \tag{6.20}$$

This implies that the magnitude of the force given by Eq. 6.7 depends upon both an atom's position in space and upon the orientation of its total atomic magnetic moment.

I will limit the discussion to an atom at rest, making the last term in Eq. 6.20 zero. I still have not described a configuration that would make an atom more likely to absorb a photon from a laser beam traveling to the right or to the left. In order to trap atoms at the origin, the experimental setup must make an atom at $x < 0$ more likely to absorb a photon from a laser beam propagating in the $+\hat{x}$ direction. Similarly, an atom at $x > 0$ should be more likely to absorb from a laser beam

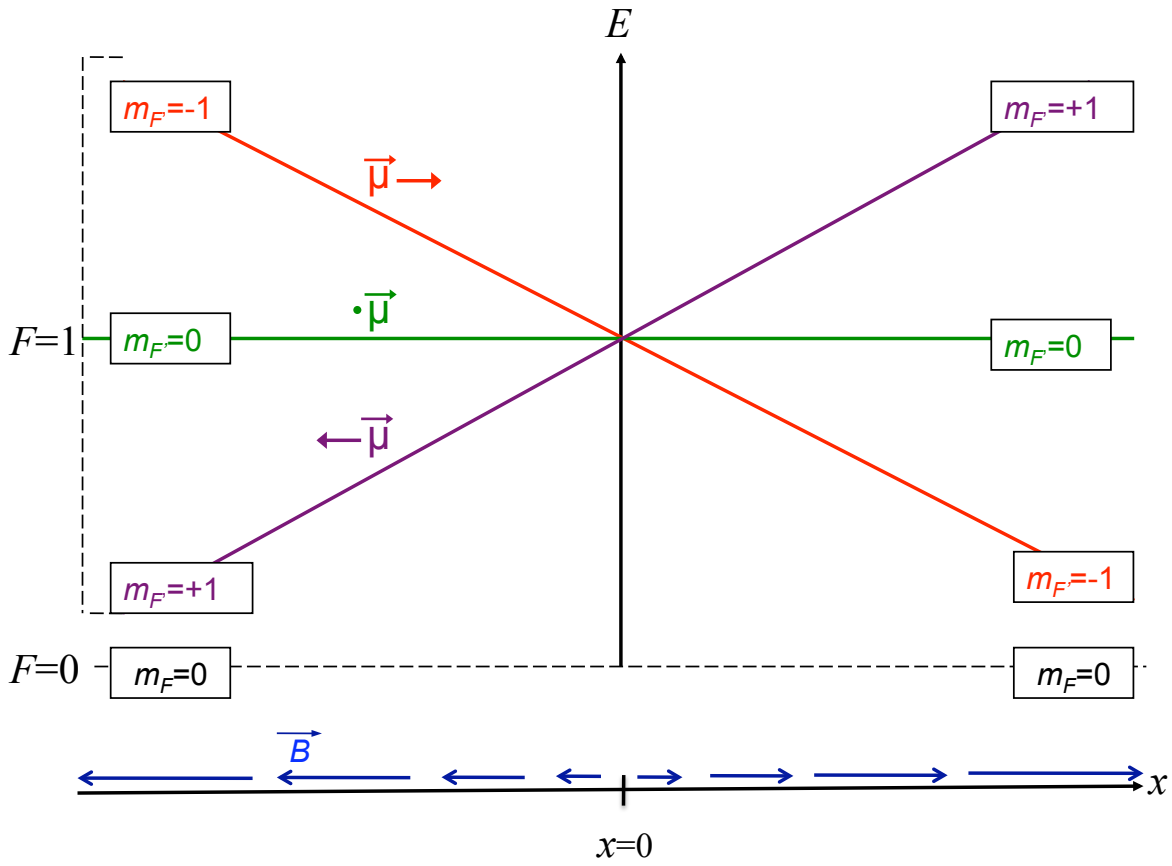

Figure 6.5: Schematic showing the spatial dependence of the Zeeman-shift in the energy of hyperfine structure states for three different orientations of the total atomic magnetic moment: one in the $+\hat{x}$ direction (red), one perpendicular to $\vec{B}_{ext}$ (green), and one in the $-\hat{x}$ direction (violet). The energy splittings are not to scale.

propagating in the $-\hat{x}$ direction. The answer to this problem lies in the conservation of angular momentum in photon-atom interactions.

In a MOT experimental setup, circularly polarized radiation is used because, unlike linearly polarized radiation, circularly polarized radiation (section 2.2) has angular momentum in addition to linear momentum. Recalling the selection rules for atomic transitions within an atom's hyperfine structure, left circularly polarized radiation (σ^+) drives a transition with a change in the total atomic magnetic moment quantum number $\Delta m_F = +1$, right circularly polarized radiation (σ^-) drives transitions with $\Delta m_f = -1$, and linearly polarized radiation excites atoms so that $\Delta m_F = 0$. [18] [4]

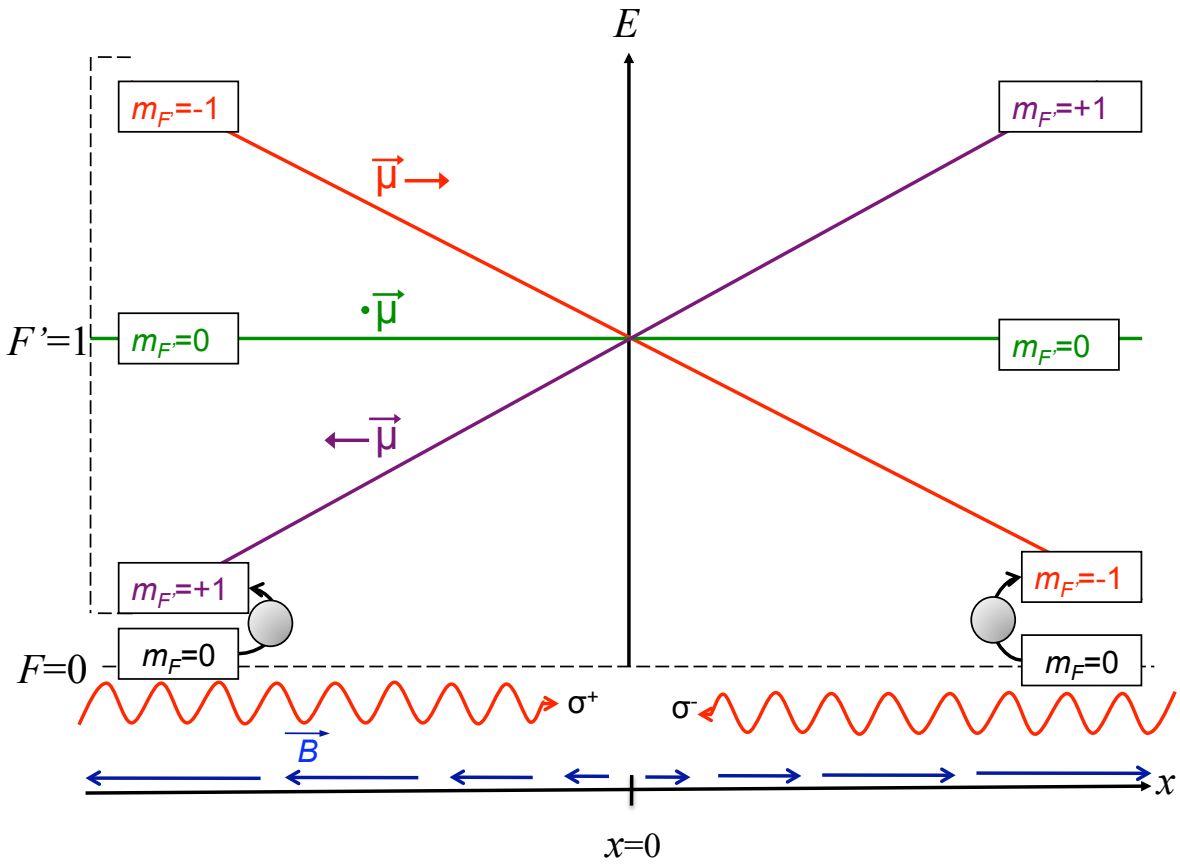

Figure 6.6: Conservation of momentum dictates from which beam an atom with Zeeman-shifted energy levels will absorb a photon.

If counter-propagating σ^- and σ^+ beams are incident upon ground state atoms, as in Fig. 6.6, then a given atom is more likely to absorb from one beam than the other. Consider, for example, an atom in the ground state at $x < 0$ with total atomic magnetic moment pointing in the $-\hat{x}$ direction. The selection rules for absorption dictate that $\Delta m_F = 0, \pm 1$. Figure 6.6 shows that the next highest excited state energy is the $(F' = 1, m_{F'} = +1)$ state. If the laser detuning Δ_0 matches the detuning due to the magnetic field $\vec{\mu} \cdot \vec{B}_{ext}$, then the atom will absorb σ^+ radiation and undergo the transition to the $(F = 1, m_F = +1)$ state. According to Eq. 6.6 an atom absorbing a photon from a laser beam propagating in the $+\hat{x}$ direction will experience a force in the same direction. Thus, the atom in this example experiences a force toward the center. By a similar argument, an atom at rest at $x > 0$ will experience a force

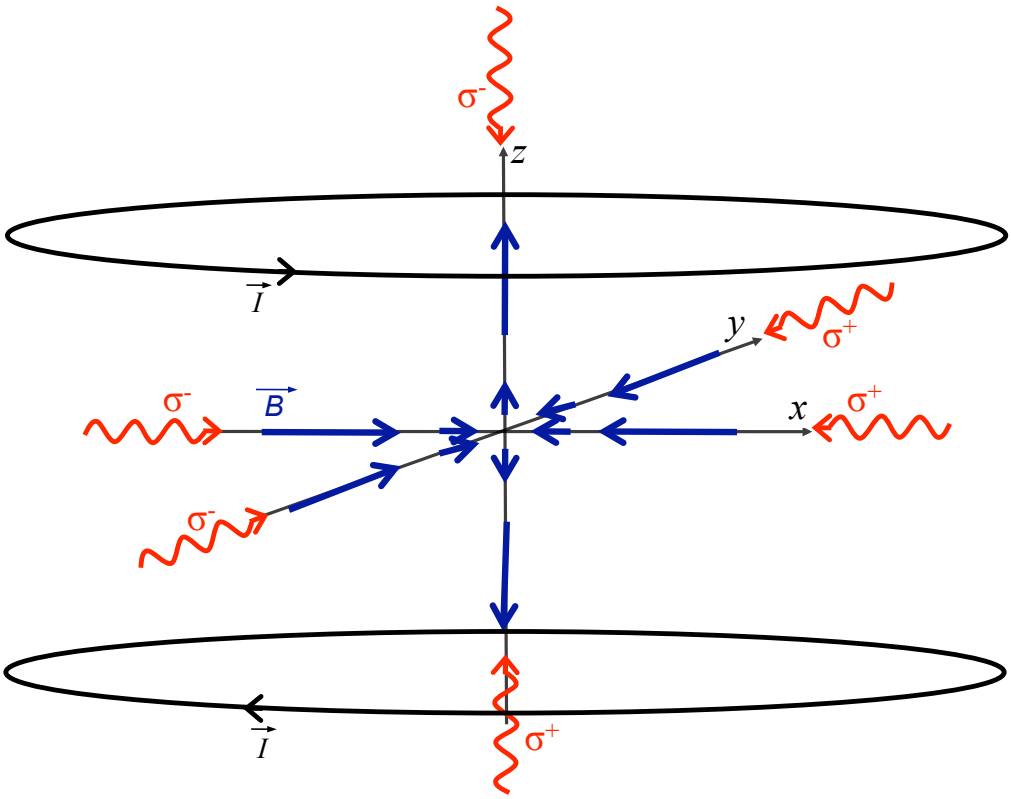

Figure 6.7: A typical MOT configuration using anti-Helmholtz coils to generate a magnetic field. The field lines represent the field lines close to the center of the trap, where the field strength can be approximated as linear.

to the left, toward the center. In this way, the magnetic field in a MOT creates a spatially-dependent restoring force for atoms in the gas.

This scheme can be readily extended to three dimensions. A pair of anti-Helmholtz coils generate the magnetic field, as shown in Fig. 6.7, which is approximately linear near the center of the trap. Beams of σ^- and σ^+ counter-propagate along the three orthogonal axes in a cartesian coördinate system in this magnetic field configuration. This configuration creates a three-dimensional restoring force on the atoms in the trap. The future goals of this project include the implementation of a trap like this one.

Appendix A

Intrinsic Carrier Concentration in Semiconductors

In section 3.1.1, we make reference to the intrinsic carrier concentration, which we find by first deriving an expression for the density of states. The density of states for electrons in the conduction band $D_e(E)$ counts the number of states in an energy range dE. To find the density of states, we first solve Eq. 3.10,

$$E_F = \frac{\hbar^2}{2m_e^*}\left(3\pi^2\frac{N}{V}\right)^{2/3},$$

for N and then differentiate with respect to an energy E_2 in the conduction band.[1] The result

$$\frac{dN}{dE_2} = D_e(E_2) = \frac{V}{2\pi^2}\left(\frac{2m_e^*}{\hbar^2}\right)^{3/2}(E_2 - E_C)^{1/2}, \tag{A.1}$$

gives us the number of states found in an infinitessimal range of condution band energies, between E_2 and $E_2 + dE_2$. To count the number of states per unit volume in the conduction band, we integrate the density of states times the probability of

[1] I introduce this notation because, although E_2 is simply a variable of integration here, this notation clarifies results in section 3.2.1.

occupancy of a given state over all energies within the conduction band:

$$n \equiv \frac{N}{V} = \frac{1}{V}\int_{E_C}^{\infty} D_e(E_2) f(E_2) dE_2. \tag{A.2}$$

The Fermi-Dirac distribution (Eq. 3.8) describes the probability that an electron has an energy E_2 in the conduction band, $E_2 \geq E_C > E_F$. At temperatures close to room temperature, $k_B T \ll E_2 - E_F$ and we can approximate the Fermi-Dirac distribution as

$$f(E) \approx \exp\left[\frac{E_F - E_2}{k_B T}\right]. \tag{A.3}$$

This assumption is valid when the Fermi level lies within the band gap, several factors of $k_B T$ away from both the conduction and valence bands. Such a condition implies that the electrons in the conduction band are in thermal equilibrium amongst themselves, as are the holes in the valence band, and the holes and electrons are in thermal equilibrium with one another. In this case, the semiconductor is simply said to be in thermal equilibrium. Performing the integration in Eq. A.2 yields

$$n = 2\left(\frac{m_e^* k_B T}{2\pi\hbar^2}\right)^{3/2} \exp\left[\frac{E_F - E_C}{k_B T}\right]. \tag{A.4}$$

Here we see that the conduction band electron density has a somewhat complicated temperature dependence, but that the temperature term in the exponent dominates this dependence. Consequently, we expect the density of states $D_e(E)$ to be higher for low temperatures.

When the Fermi level is in the band gap, several values of $k_B T$ away from the valence band edge ($k_B T \ll E_F - E_V$), we can also determine the hole concentration. Given this condition, the probability of occupancy for a hole in the valence band with

some energy $E_1 < E_F$ is

$$1 - f(E_1) \approx \exp\left[\frac{-(E_F - E_1)}{k_B T}\right]. \tag{A.5}$$

By a similar derivation, the density of states for holes in the valence band is

$$D_h(E_1) = \frac{V}{2\pi}\left(\frac{2m_h^*}{\hbar^2}\right)^{3/2}(E_V - E_1)^{1/2}. \tag{A.6}$$

This can be derived by an argument similar to that of Eq. A.1 using the effective mass of a hole m_h^*. Now, counting the number of hole states P per unit volume in the valence band, we integrate the density of states times the hole occupation probability over all energies within the valence band

$$p \equiv \frac{P}{V} = \frac{1}{V}\int_{-\infty}^{E_V} D_e(E_V - E_1)\,(1 - f(E_1))\,dE_1 \tag{A.7}$$

$$= 2\left(\frac{m_h^* k_B T}{2\pi\hbar^2}\right)^{3/2}\exp\left[\frac{E_V - E_F}{k_B T}\right]. \tag{A.8}$$

The law of mass action states that, at equilibrium, the product of n and p must be a constant, which we define as the square of the intrinsic concentration n_i:

$$np \equiv n_i^2. \tag{A.9}$$

Taking the square root of the hole and electron concentrations

$$n_i = 2\left(\frac{k_B T}{\hbar^2}\right)^{3/2}(m_e^* m_h^*)^{3/4}\exp\left[\frac{E_g}{2k_B T}\right], \tag{A.10}$$

where $E_g = E_V - E_C$, yields a formulation for intrinsic carrier concentration that is independent of Fermi level energy E_F.

Appendix B

The Lorentz Model

Recall that, in section 4.2, we equated all of the forces on an electron in the Lorentz Model: the spring force, the frictional damping force, and the force on the charge due to the electric field of an electromagnetic wave. Beginning with the differential equation of motion for this situation, Eq. 4.12,

$$\frac{d^2x}{dt^2} + \gamma\frac{dx}{dt} + \omega_0^2 x = \frac{q}{m_e}E_0 cos(\omega t), \tag{B.1}$$

the steady state solution to the differential equation is oscillatory $\tilde{x}(t) = \tilde{x}_0 \exp[-i\omega t]$, where $\tilde{x}$ is used to denote a complex quantity. Substituting this solution into Eq. B.1, we find that

$$\tilde{x}_0 = \frac{q/m_e}{\omega_0^2 - \omega^2 - i\gamma\omega}E_0.$$

The electric dipole moment $p(t)$ of the atom is the real part of the expression

$$\tilde{p}(t) = q\tilde{x}(t) = \frac{q^2/m_e}{\omega_0^2 - \omega^2 - i\gamma\omega}E_0 e^{-i(\omega t - kz)}. \tag{B.2}$$

In Chapter 2, the atomic polarizability α was defined as the proportionality constant between electric dipole moment and electric field. In the case of the dipole moment given in Eq. B.2, there is no real atomic polarizability that can describe the relation-

ship between the electric field and the dipole moment. This is because the dipole moment lags behind the electric field by an angle of arctan $\left[\frac{\gamma\omega}{(\omega_0^2-\omega^2)}\right]$.

There is, however, a complex polarizability $\tilde{\alpha}(\omega)$ that can describe the relationship

$$\tilde{p}(t) = \tilde{\alpha}(\omega)\tilde{E}(t), \tag{B.3}$$

in which the complex polarizability

$$\tilde{\alpha}(\omega) = \frac{q^2/m_e}{\omega_0^2 - \omega^2 - i\gamma\omega}. \tag{B.4}$$

The complex polarization is simply the polarizability multiplied by the number of atoms in a given volume of the gas, N.

$$\vec{\tilde{P}}(t) = N\tilde{\alpha}(\omega)\vec{\tilde{E}}(t). \tag{B.5}$$

This formulation allows us to use the wave equation in terms of polarization (Eq. 2.6),

$$\nabla^2\vec{\tilde{E}}(t) - \frac{1}{c^2}\frac{\partial^2\vec{\tilde{E}}(t)}{\partial t^2} = \frac{1}{\epsilon_0 c^2}\frac{\partial^2\vec{\tilde{P}}(t)}{\partial t^2}.$$

Substituting the complex polarization $\vec{\tilde{P}}(t)$ of Eq. B.5 and solving for k^2, we find that k must satisfy the dispersion relation

$$k^2 = \frac{\omega^2}{c^2}\left(1 + \frac{N\tilde{\alpha}(\omega)}{\epsilon_0}\right). \tag{B.6}$$

From Eq. B.6 we can recognize the quantity

$$n(\omega) = \left(1 + \frac{N\tilde{\alpha}(\omega)}{\epsilon_0}\right)^{1/2} \tag{B.7}$$

$$= n_{re} + in_{im} \tag{B.8}$$

as the frequency-dependent index of refraction. The dispersion relation (Eq. B.6) reveals a remarkable difference between electromagnetic radiation propagating in vacuum and that passing through a gas. Rewriting the expression for the electric field shows that the electric field is not purely oscillatory as it propagates through a gas:

$$\begin{aligned}
\vec{\tilde{E}}(z,t) &= E_0 \exp\left[-i(\omega t - kz)\right] \hat{z} && \text{(B.9)} \\
&= E_0 \exp\left[-i\omega(t - \frac{n(\omega)z}{c})\right] \hat{z} && \text{(B.10)} \\
&= E_0 \exp\left[-i\omega(t - \frac{n_{re}(\omega)z}{c})\right] \exp\left[-\frac{n_{im}(\omega)\omega z}{c}\right] \hat{z}. && \text{(B.11)}
\end{aligned}$$

The second exponential term in Eq. B.11 is a decaying exponential that depends on frequency ω and propagation distance z. In this way, the Lorentz model describes the absorption of light by a gas of atoms, with the absorption coefficient defined as the exponential decay parameter

$$\begin{aligned}
a(\omega) &\equiv \frac{n_{im}(\omega)}{c}\omega && \text{(B.12)} \\
&= \frac{Nq^2}{\epsilon_0 m_e c} \frac{\gamma\omega^2}{(\omega_0^2 - \omega^2)^2 + \gamma^2\omega^2}. && \text{(B.13)}
\end{aligned}$$

Bibliography

[1] Carl Wieman. Inexpensive laser cooling and trapping experiment for undergraduate laboratories. *Am. J. Phys*, 63(4):317–330, 1994.

[2] Peter W. Milonni and Joseph H. Eberly. *Lasers*. Wiley, New York, 1988.

[3] David J. Griffiths. *Introduction to Electrodynamics*. Prentice Hall, Upper Saddle River, NJ, 3rd edition, 1999.

[4] Alan Corney. *Atomic and Laser Spectroscopy*. Clarendon Press, Oxford, 1988.

[5] John David Jackson. *Classical Electrodynamics*. Wiley, New York, 2nd edition, 1975.

[6] Eugene Hecht and Alfred Zajac. *Optics*. Addison-Wellesley, Reading, MA, 1st edition, 1974.

[7] Amnon Yariv. *Quantum Electronics*. John Wiley and Sons, New York, 3rd edition, 1989.

[8] Charles Kittell. *Solid State Physics*. Wiley, 8th edition, 2005.

[9] Bahaa E. A. Saleh and Malvin Carl Teich. *Fundamentals of Photonics*. John Wiley and Sons, New York, 1st edition, 1991.

[10] Matthew E. Bonner. *High Resolution Study of the Output Wavelength of Diode Lasers as a Function of Diode Temperature and Injection Current.* Middlebury College Department of Physics, Middlebury, VT, 1992.

[11] Sacher Lasertechnik. *Littman Laser User's Manual: TEC 500.* Sacher Lasertechnik, Marburg, Germany, 2002.

[12] Kenneth P. Nagle. *Saturated Absorption and Intermodulated Optogalvanic Spectroscopy of a HeNe Discharge from 6678 Angstroms to 6679 Angstroms.* Middlebury College Department of Physics, Middlebury, VT, 2003.

[13] Stephen C. Bennett. *Hyperfine Structure Measurements in Atomic Sodium.* Middlebury College Department of Physics, Middlebury, VT, 1992.

[14] Richard Wolfson. *Essential University Physics.* Pearson Education, Inc., San Francisco, CA, 1st edition, 2007.

[15] Robert Eisberg and Robert Resnick. *Quantum Physics of Atoms, Molecules, Solids, Nuclei, and Particles.* John Wiley and Sons, Hoboken, NJ, 2nd edition, 1985.

[16] Paul A. Tipler and Ralph A. Llewellyn. *Modern Physics.* W.H. Freeman and Company, New York, 5th edition, 2008.

[17] *Optical Pumping of Rubidium.* unpublished laboratory manual, Madison, WI, 2005.

[18] Daniel Adam Steck. *Rubidium 85 D Line Data.* Oregon Center for Optics and Department of Physics, University of Oregon, 2010. http://steck.us/alkalidata/.

[19] Daniel Adam Steck. *Rubidium 87 D Line Data.* Oregon Center for Optics and Department of Physics, University of Oregon, 2010. http://steck.us/alkalidata/.

[20] Harold J. Metcalf and Peter van der Straten. *Laser Cooling and Trapping*. Springer-Verlag, New York, 1999.

[21] Anne Goodsell. *Capture of Laser-Cooled Atoms with a Carbon Nanotube*. Ph.D. Dissertation, Harvard University, Department of Physics, 2010.

[22] S Cauchi et. al. Absorption spectroscopy of trapped rubidium atoms. *Can. J. Phys.*, 82:905–916, 1992.

[23] Kelvin Wagner. *Doppler-Free Saturated Absorption Spectroscopy: Laser Spectroscopy*. Unpublished laboratory manual, Department of Electrical and Computer Engineering, University of Colorado, Boulder, CO, 2010.

[24] W.M. Hayes. *CRC Handbook of Chemistry and Physics*. CRC Press, New York, 91st edition, 2010.

[25] C. Wieman K.B. MacAdam, A. Steinbach. A narrow-band tunable diode laser system with grating feedback, and a saturated absorption spectrometer for cesium and rubidium. *Am. J. Phys.*, 60(12):1098–1111, 1992.

[26] David A. Smith and Ifan G. Hughes. The role of hyperfine pumping in multilevel systems exhibiting saturated absorption. *Am. J. Phys.*, 72(5):631–637, 2004.

[27] P. D. Lett et al. Optical molasses. *Journal of the Optical Society of America*, 6(11):2084–2107, 1989.